Sediment flux and early diagenesis inferred from high-resolution XRF-CS data and iron and arsenic sulfides during the last 30 kyr in Lake Urmia, Iran: Implications for studies of hypersaline lakes

Ting Kong, Alina Tudryn, Elisabeth Gibert-Brunet, Piotr Tucholka, Seyed-Hani Motavalli-Anbaran, Mohammad Lankarani, Hesam Ahmady-Birgani, Serge Miska, Gilda Karimi, Olivier Dufaure

Sediment flux and early diagenesis inferred from high-resolution XRF-CS data and iron and arsenic sulfides during the last 30 kyr in Lake Urmia, Iran: implications for studies of hypersaline lakes.

Ting Kong[a], Alina Tudryn[a,*], Elisabeth Gibert-Brunet[a], Piotr Tucholka[b], Seyed-Hani Motavalli-Anbaran[c], Mohammad Lankarani[d], Hesam Ahmady-Birgani[e], Serge Miska[a], Guilda Karimi[f], Olivier Dufaure[a]

[a] University Paris-Saclay, CNRS, UMR 8148-GEOPS, 91405, Orsay, France

[b] Faculty of Geology, Warsaw University, Warsaw, Poland

[c] Institute of Geophysics, University of Tehran, Tehran, Iran

[d] School of Geology, University-College of Science, University of Tehran, Tehran, Iran

[e] Faculty of Natural Resources, Urmia University, Urmia, Iran

[f] Faculty of Biological Sciences, Kharazmi University, Tehran, Iran

[*] *corresponding author: alina.tudryn@universite-paris-saclay.fr*

Abstract

We analyzed by high resolution X-ray fluorescence core scanning (XRF-CS) the elemental composition of a 12.5 m long composite sediment core extracted from the hypersaline Lake Urmia (NW Iran). The main objective of the study was to reconstruct on a high temporal scale,

the changes in sediment origin/inflow and water levels of Lake Urmia over the last 30,000 years. Combined with previously obtained results on ^{14}C accelerated mass spectrometry (AMS) chronology, grain size and distribution of major minerals, albeit with a much lower temporal resolution than the XRF-CS data, this multi-proxy approach allowed recognition of specific hydrological changes and associated sedimentary processes in the Lake Urmia basin, including physical and chemical weathering, depositional fluxes and carbonate crystallization processes in lake water, and early diagenesis in anoxic bottom sediments. The high natural logarithm ratios (ln-ratios) of K/Ti, Ca/Ti and Sr/Ca, and low ln-ratios of Rb/Sr reveal increasing chemical weathering in the catchment area in conjunction with increasing authigenic carbonate precipitation in the lake. These findings reflect wet conditions, high lake levels and less saline water during the following intervals (i) 29.8-20.2, (ii) 15.2-13.3, (iii) 11.8-5.6 and (iv) 4.1-2.3 cal kBP.. In contrast, the increasing ln-ratios of Rb/Sr associated with decreasing ln-ratios of K/Ti, Ca/Ti and Sr/Ca indicate enhanced erosion in the catchment area linked to drier conditions, lower lake levels and more saline conditions predominating at around 30-29.8 cal kBP, 20.2-15.2, 13.3-11.8, and 5.6-4.1 cal kBP.. Based on the As-XRF-CS pattern and magnetic parameters we identified iron and naturally-occurring arsenic sulfides rarely reported from saline lakes, acting as specific indicators of anoxic conditions in the lake bottom environment. Moreover, XRF-CS data revealed short-lived periods with increasing chemical weathering in the catchment area at (i) 28.6-28.3, (ii) 27.3-27.1, (iii) 4.1-3.6 and (iv) 3.4-3.3 cal kBP, as well as increasing erosion at (i) 27.0-26.8, (ii) 26.3-26.0, (iii) 25.6-25.3 and (iv) 24.6-24.4 cal kBP.. Overall, this study confirms the previously reported findings concerning the sediments of Lake Urmia as well as completing these, both by providing more details on

45 the environment for the periods already identified and by highlighting events of short duration.
46 In particular, the results reported here permit better definition of the processes of chemical
47 weathering *versus* erosion in the catchment area, and of the oxygenation levels of the lake
48 bottom. The close correlation of these long- and short-term changes with the North Atlantic
49 climate system clearly indicates that the Lake Urmia area has been affected mainly by this
50 system during the last 30 cal kBP.
51 Over and above their value with regard to Lake Urmia, these new data fill an important gap in
52 eastern Mediterranean/western Asia paleoclimate records as a whole, providing unique and
53 continuous 30 cal kBP information on the possible driving mechanisms of the observed
54 changes. These can be compared to existing data on paleoenvironmental and climatic changes
55 on regional and global scales and can also be used in global circulation models.
56
57 Keywords: XRF CS geochemistry; iron and arsenic sulfides; early diagenesis; anoxic
58 environment; short-time climate change, environmental sedimentology; paleoclimatology;
59 salty lake.
60
61 **1. Introduction**
62 The study of continents directly and significantly contributes to the understanding of climate
63 change affecting densely populated geographical regions, especially with regard to ensuring
64 accessibility to natural water resources in arid and semi-arid climate zones. Among the various
65 continental markers, lakes provide access to both local-scale conditions and regional-scale
66 climate change with a high temporal resolution. Cored lake sequences therefore constitute

reliable paleoenvironmental records, characterized by a signal that is often continuous and sensitive over time. This applies especially to closed lake basins in which variations in the water balance are essentially and/or directly linked to climatic fluctuations. In studies on the sediments of these closed basins, geochemical analyses by scanning X-ray fluorescence (XRF) spectrometry enable the interpretation of past environmental and climatic changes with the advantages of both sample preservation and the possibility of obtaining a continuous high-resolution record of elemental composition (Croudace et al., 2019; Evans et al., 2019; Guo et al., 2021; Hennekam et al., 2019; Peti and Augustinus, 2022).

The elemental composition of lake sediments is controlled by (i) the geochemistry of the detrital input, which is in turn determined by geology and hydrodynamic sorting, (ii) the history of weathering and erosion on the watershed, and (iii) the various sedimentary processes occurring in the water column and at the water-sediment interface. The combination and comparison of several high-resolution XRF data sets provide information on (i) detrital inputs through analyses of elements such as Ti, Fe, Si, Al, Rb and K (Croudace and Rothwell, 2015; Davies et al., 2015; Kylander et al., 2011), (ii) chemical weathering and erosion of watersheds, the K/Ti ratio for example (Xie et al., 2014), (iii) the composition and content of the carbonate procession and the variations in evaporates, when present, based on elements such as Ca, Sr and S, and ratios such as Ca/Ti, Sr/Ca (Davies et al., 2015), and (iv) the salinity of the lake water in terms of chlorine (Cl), in studies on saline lakes (Brisset et al., 2018).

Despite having been the world's second largest hypersaline lake for years, Lake Urmia (western Iran) has experienced significant changes in its water level, that rapidly fell from 1278 to 1270 m above sea level (a.s.l.) from 1994 onward. Since Lake Urmia is a closed basin, the

89 main causes of this pronounced 8-m drop in lake level were likely a decrease in riverine inflow
90 and/or excess evaporative outflow, which could have been caused by anthropogenic alterations
91 including dam construction, channel deviation, groundwater pumping (Tourian et al., 2015), as
92 well as climate change involving reduced precipitation and/or increased temperatures.
93 Although anthropogenic factors have been widely discussed (Ahmady-Birgani et al., 2020;
94 Asem et al., 2019; Chaudhari et al., 2018; Khazaei et al., 2019), the lack of high-resolution
95 sedimentary records in the past limits our understanding of ongoing processes in the context of
96 present-day climate variations. Existing data either cover a very long time scale but with low
97 resolution, or are discontinuous, or concern a very short-term period (Djamali et al., 2008a;
98 Kelts and Shahrabi, 1986; Stevens et al., 2012; Talebi et al., 2016).
99 Within the framework of the Lake Urmia project (Tudryn et al., 2021) various mineralogical
100 studies have been undertaken, analyzing lacustrine cored sequences, with the aim of
101 deciphering the patterns and trends of the lake's past environmental evolution in relation to
102 natural *versus* anthropogenic impacts and integrating the results into sustainable water and
103 ecosystem management strategies. However, the environmental changes over the last 30
104 millennia recently elucidated and discussed (Kong et al., 2022), were based on data
105 characterized by a much lower temporal resolution compared to X-ray fluorescence core
106 scanning (XRF-CS analyses). In this report, we present the results of XRF-CS analyses
107 performed on these lacustrine sequences. The objectives of this study were (i) to obtain new
108 clues concerning the evolution of the lake, based on XRF-CS elemental data, after their
109 calibration as environmental indicators by correlations with the mineralogical data already
110 obtained (Tudryn et al., 2021; Kong et al., 2022), and (ii) to reconstruct on a high temporal

111 scale the evolution of sediment origin/influx and levels of Lake Urmia over the past 30,000
112 years. Finally, the results obtained will help to better understand the climate change at a more
113 regional to global scale during the late Pleistocene and the Holocene.
114
115 **2. General setting**
116 Lake Urmia is a shallow, perennial hypersaline lake located in the lowest part of an endorheic
117 depression in northwestern Iran, in the province of Azerbaijan, near the Turkish and Iraqi
118 borders (Fig. 1). It is located approximately at a longitude between 45°00' and 46°00' east and
119 a latitude of 37°00' and 38°16' north, at an altitude of 1270 m a.s.l.. The lake is surrounded by
120 the Zagros and Alborz Mountain ranges, rising to a maximum elevation of 3155 m a.s.l. in the
121 north, 3608 m a.s.l. in the west, 3332 m a.s.l. in the south, and 3850 m a.s.l. in the east (Jalili
122 et al., 2012). Prior to the recent fall in lake level starting in the mid-1990s, Lake Urmia had a
123 water level of 1278.4 m a.s.l., a depth of 8-12 m and a surface area of 5700 km^2 (with a length
124 of 140 km and a width of 15-50 km) and was considered to be the second largest salty lake on
125 earth after the Caspian Sea (Shahrabi, 1981; Kelts and Shahrabi, 1986). Before this drop in
126 level, Lake Urmia salinity varied between 140 and to 220 $g.L^{-1}$ on an annual basis (Bottema,
127 1986; Eimanifar and Mohebbi, 2007; Sharifi et al., 2018). According to Alipour (2006), the
128 major cations present in the lake water includes Na^+, Mg^{2+}, Ca^{2+} and K^+ while the major anions
129 were Cl^-, SO_4^{2-} and HCO_3^-. The catchment area of the lake extends over 52,000 km^2 (Sharifi et
130 al., 2018). Thirteen primary inflows from the surrounding mountains supply the lake, majority
131 of this water supply coming from Zarrineh Rud to the south of Lake Urmia. The decline in lake

132 level to 1270.85 m in 2019, reducing the lake's surface area to 2400 km^2, resulted in a rise in
133 salinity reaching values of up to 380 $g.L^{-1}$ (Sharifi et al., 2018; Ahmady-Birgani et al.2020).
134 Lake Urmia lies on the Turkish-Iranian plateau, the center of the Arabian-Eurasian collision
135 zone within the Alpine-Himalayan orogenic belt, where crustal deformation since the Late
136 Miocene has been dominated by a N-S shortening associated with an E-W extension (Berberian
137 and Arshadi, 1976; Solaymani Azad, 2009; Allen et al., 2013). This deformation has resulted
138 in faults, earthquakes and the specific distribution of volcanoes forming the highest mountains
139 on the plateau. Lake Urmia corresponds to a tectonic depression associated with the movement
140 of large fault zones. The Tabriz Fault System lies to the N-E of Lake Urmia, and to the east of
141 the lake, the Sahand volcano (3695 m a.s.l.), the third highest volcano on the Turkish-Iranian
142 plateau, dominates the landscape (Fig. 1c). The active Zagros thrust zone is located west of the
143 lake (at a distance of ~100 km).
144 The lake basin is composed of a variety of rock formations ranging from Precambrian
145 metamorphic complexes to Quaternary mud deposits as presented in Fig. 1c. Paleozoic
146 metamorphic rocks characterize the Zagros Mountains in the west of the basin while intrusive
147 rocks occur in the southern, western, and northwestern areas of the basin and volcanic to
148 volcano-sedimentary formations dominate in the eastern and northeastern basin. In addition,
149 carbonate sedimentary units prevail in the southern and western basin, whereas the northeastern
150 basin is characterized by the presence of evaporitic sedimentary units (Kelts and Shahrabi,
151 1986).
152 The Lake Urmia catchment area is mainly influenced by the Mediterranean climate
153 characterized by hot and dry summers and cold and wet winters in the Eastern Mediterranean

and Anatolia regions (Finné et al., 2011). In winter, the penetration of westerlies bringing humid air masses from the North Atlantic and the Mediterranean towards the continental interior as far as western Iran is controlled by the strength of cold, dry winds from the Siberian high in the north-east (Alijani and Harman, 1985; Stevens et al., 2001; Kehl, 2009). In summer, the subtropical high-pressure belt extends over nearly the whole of Iran, resulting in north-easterly winds and hot, dry conditions (Stappen et al., 2001). The climate of Lake Urmia is also influenced by the surrounding mountains and orographical barriers, specifically the Alborz Mountains, which limit the inflow of humid air from the Caspian Sea to the lake area.

3. Material and methods

3.1 Sediment cores and sampling

In September 2017, three sediment cores, namely Golman 5 (5.25 m long; 37°35'33.4'' N, 45°16'27.6'' E), Golman 6 (8.0 m long; 37°35'28.8'' N, 45°16'33.8'' E;) and Golman 7 (12.5 m long; 37°35'28.7''N, 45°16'33.7''E), were extracted from the mouth of the Shahr Chay River in the recently dried out part of the west coast of the lake near the city of Urmia (Fig. 1d, Tudryn et al., 2021). The cores were extracted in close proximity to one another, at a distance from today's shoreline to ensure safe use of a mechanical corer, and by borehole casing. Coring was stopped when gas with an intense H_2S odor rose up from the Golman 6 and Golman 5 boreholes and pressurized water with mud and gas with the same odor rose up from the Golman 7 borehole to the lake surface. Below the surface crust, the uppermost sediments were soft and sandy at the coring site. The first section of all cores was therefore collected in the form of a

compacted and incomplete sequence that we could not include in the study. In addition, due to the presence of interbedded captured water (either residual water from the sediment or ancient lake water trapped within the deposits), the 4.20 to 8.65 m section of the Golman 7 core was too wet to be retrieved by the corer, resulting in an empty section for this depth interval. Core sections up to 1 m long and preserved in plastic tubes were transported to the GEOPS laboratory (University Paris-Saclay, France) and stored in a cold room. For sampling, the cores were cut longitudinally into two parts: one was kept as an archive, while parallel U-channels and several discrete samples were taken from the other one. Tight sealing of the U-channels enabled good preservation of the sediment and measurements were performed soon after sampling and therefore on fresh material. The two longest cores, Golman 6 and Golman 7, which had been studied previously, showed the same lithological succession, as well as changes in carbonate content and magnetic susceptibility (Tudryn et al., 2021) and were used to construct the 12.5 m long composite core (Kong et al., 2022). The results presented in this study were derived from this composite core. Collected in the same area, the Golman 5 core duplicated the most recent part of the composite sequence and the main peaks, especially for magnetic susceptibility and carbonate contents, were fully correlated (for details, see Tudryn et al., 2021).

3.2. Identification of the elemental composition of bulk sediments

The elemental composition of bulk sediments was non-destructively analyzed every 5 mm on the U-channel core using a fourth generation Avaatech XRF core scanner (LSCE Laboratory, GEOPS/LSCE PANOPLY platform, Gif sur Yvette, France). Before the measurements were made, the surface of the sediment in each section was carefully smoothed and covered with 4-

μm thick Ultralene foil to protect the measurement triangle and prevent desiccation of the sediment. Elemental intensities were obtained at 10 kV (with a current of 200 μA, no filter, and under helium flow) for the light elements (Mg, Al, Si, P, S, Cl, K, Ca, Ti), and at 30 kV (with a current of 150 μA, a thin Palladium filter, and under air) for the heavier elements (Mn, Fe, Ni, Cu, Zn, As, Br, Rb, Sr, Zr). The measurement window was 5 mm (downcore) by 10 mm (crosscore), and the counting time was 10 s for each target sample and both runs. The SARM4 certified standard, the so-called "Monitor scan", was measured at 10 kV between each core section analysis to ensure that there were no technical problems with the scanner (such as a helium leak that could affect the counts of light elements).

The chemical composition of the sediment was measured by the XRF scanner as element intensities expressed in total counts (cnts). The relative changes in elemental data based on XRF-CS results, were recorded as elemental profiles, rather than as absolute concentrations. Statistical analyses to construct the item correlation matrix and principal component analysis (PCA) were performed using Orange software and calculated automatically.

According to Weltje and Tjallingii (2008) and Weltje et al. (2015), raw elemental intensities obtained from XRF-CS data do not have a unique relationship to sediment composition. However, these authors showed that natural logarithm ratios (ln-ratios) of element intensities are related to ln-ratios of element abundances, thus providing easily interpretable signals of relative changes in chemical composition and minimizing the risk of drawing erroneous conclusions from geochemical proxies. Since our aim was to identify relative changes in the nature and abundance of fluxes of lacustrine and continental material, we present the results as ln-ratios intensities.

221

222 3.3. Identification of evaporate minerals: gypsum and halite

223 Mineralogical components was identified on 49 samples by X-ray diffraction (XRD) on
224 whole sediment powder at the GEOPS laboratory (Paris-Saclay University, GEOPS/LSCE
225 PANOPLY platform, Orsay, France). The XRD pattern was recorded using an X'Pert Pro
226 PANalytical diffractometer, with a Cu-Kα source, 2Θ range 5°–80°, in 4-h runs. Gypsum and
227 halite were identified using PANalytical HighScore software and an open crystallography
228 database in the GEOPS laboratory. Gypsum and halite were semi-quantified by normalizing
229 their diffraction peak areas (gypsum: 7.5 Å; halite: 2.8 Å) to the area of the main quartz peak
230 (3.34 Å) and the percentage areas of the main minerals identified in the sample (Kong et al.
231 2022).

232

233 **4. Previous studies on the composite core**

234

235 Two scientific papers have been published so far in the framework of the Franco-Iranian project
236 on Late Pleistocene-Holocene Lake Urmia, both concerning water and sediment samples taken
237 from the catchment area and lake deposits (Tudryn et al., 2021; Kong et al., 2023). The results
238 obtained on lake sediments from the composite core constructed by Kong et al. (2022) are
239 summarized here with emphasis on lithology, the time scale established and mineralogy. As
240 our research was conducted on the same composite core, these data form the basis for our
241 results.

242

243 4.1. Lithology

The composite sedimentary sequence consists of two well individualized lithological units between 12.50 and 1.60 cm depth (Fig. 2). The lower unit 1 extending from 12.50 to 4.52 m depth, began with subunit 1a, starting from the base of the core at a depth of 12.50 m to 12.38 m. This subunit was composed of brownish sand followed by a black and dark gray layer, rich in plant remains, at depth of 12.48–12.43 m, with a gray silt above (Fig. 2). In subunit 1b, extending from 12.38 to 4.52 m depth, the sediment was highly water-rich and consisted of gray silty/clayey deposits with some 1-mm thick sandy layers and a layer between 8.87 and 8.65 m with increased contents of silt and sand. The transition from unit 1 to upper unit 2 was marked by a clear change at a depth of 4.52 m. Unit 2 extended up to the core-top at 1.60 m and was compact and heterogeneous, with alternation of sands, silts and clays of different colors. Its subunits were clearly differentiated as follows: (i) subunit 2a, between 4.52 and 4.02 m depth, consisted of brown sand and silt, (ii) subunit 2b, from 4.02 to 3.85 m in depth, comprised homogeneous gray clay and fine silt, (iii) subunit 2c, between 3.85 and 3.73 m in depth, contained gray and dark gray sand, (iv) subunit 2d, at 3.73–2.87 m in depth, comprised homogeneous gray clay and fine silt containing an abundance of fecal pellets corresponding to the development of the brine shrimp *Artemia urmiana* in the lake. This subunit began and ended sharply, with approximately 2 cm thick quite dry, light gray clay clearly separated from the subunits above and below, and was softer in the middle, (v) subunit 2e, extending from 2.87 to 2.20 m in depth, consisted in sandy and silty layers, starting with an 8-cm thick dark gray and black layer rich in organic remains including plant fragments, and (vi) subunit 2f, extending from 2.20 to the core top at 1.60 m in depth, and comprising gray sand and silt containing varying concentrations of fecal pellets of the brine shrimp *Artemia urmiana*.

266

267 4.2. Age model

268 The time-scale was defined by 11 AMS ^{14}C dating of both organic fractions, including diffused
269 organic matter and hand-picked charcoal, and inorganic and biomediated (*i.e.,* fecal pellet)
270 carbonates (Fig. 2). Taking into account all the data concerning the carbonate fraction in the
271 composite core and in the catchment area, as well as those relating to the hydrogeochemical
272 system of the lake, we applied two age corrections: (i) related to the detrital fraction of
273 carbonates in the dated samples, and (ii) taking into account the hard water effect (HWE),
274 considering that authigenic materials such as inorganic carbonates and organic matter are
275 formed in the upper layer of the lake water. This hard water effect was quantified with regard
276 to recent years (*i.e.* 0.4 kyr) by the ^{14}C activity of the total dissolved inorganic carbon (TDIC)
277 measured on the lake water, and in the more distant past (*i.e.* around 2 kyr), by the comparison
278 of the ages determined at the same level on carbonate and charcoal, the latter being considered
279 as strictly authentic and disconnected from the geochemical age of the water. The second, 2
280 kyr, correction applied to carbonate and organic matter dating combined these two HWE
281 effects, including the modern HWE.

282 From 12.5 to 4.52 m in depth, ^{14}C AMS chronology is based on four datings that are in
283 agreement with the lithostratigraphy, with a measured sedimentary rate (msr) of 0.9 $mm.yr^{-1}$.
284 From a depth of 4.52 m to the core top, two phases were distinguished, corresponding to depth
285 of 4.52–2.87 m and 2.87–1.6 m respectively, associated with a msr of 0.1 and 0.4 $mm.yr^{-1}$
286 respectively (Fig. 2).

287

4.3. Previous core analyses

Previous sediment analyses included parameters such as (i) magnetic susceptibility, hysteresis loop and Curie temperature allowing estimation of the nature and contents of ferromagnetic minerals in the sediment (Tudryn et al., 2021), (ii) grain size, reflecting transport energy or distance from detrital sources, and (iii) mineralogy determined by XRD allowing identification of the silicate (including clays), and carbonate fractions, and the semi-quantification of the major mineralogical species identified. Measurement step of magnetic susceptibility, grain size and clay minerals analyses was 1 cm, mineralogical species being determined every five cm or more (Kong et al., 2022).

The results clearly defined several successive environmental phases dating from 30.0 to 2.3 cal kBP (Kong et al., 2022). At about 30 cal kBP, all proxies indicated a low lake stand and even drying out at the core site, followed by an increase in water level with open conditions between 29.9 and 20.2 cal kBP *i.e.*, mainly during the Last Glacial Maximum (LGM). Thereafter, all data suggest highly unstable lake conditions. Low lacustrine stands were recorded during the intervals 20.2-15.3, 13.3-11.8 and 5.6-4.1 cal kBP whereas lake conditions recovered during the intervals 15.3-13.3, 11.8-5.6 and 4.1-2.3 cal kBP. The high lake stand recorded between 15.3 and 13.3 cal kBP is likely attributable to the Bølling–Allerød warming, whereas the following 13.3-11.8 cal kBP regressive phase probably corresponds to the Younger Dryas cooling. With regard to the Early-Mid Holocene, the high aragonite contents clearly indicated a lacustrine environment from 11.8 to 5.6 cal kBP.

5. Results and interpretations

310 To quantify the strength of the association between the elements analyzed, a correlation matrix
311 and principal component analysis (PCA) plots were constructed (Fig. 3). Two groups of highly
312 correlated elements (correlation matrix index r>0.75) could be distinguished in the PCA plot:
313 (i) the Si group including Al, K, Ti, Fe, Zn, Mg, Mn and Rb, and (ii) the Ca–Sr group. Certain
314 other elements such as (iii) the Cl-S group, including arsenic (As), do not display clear
315 correlations, but appear to be significant component of the lake sediments as well as
316 environmental indicators.
317
318 5.1. The Si group
319 The elements in this group were highly correlated one another and showed a very similar
320 pattern of ln-ratios when plotted on a time scale and normalized against elements outside the
321 group such as Ca or Sr. For example, Si and Rb concentrations expressed as ln-ratios of Si/Ca
322 and Rb/Sr intensity variations (Fig. 4a, 4b) clearly showed the correlation between these
323 parameters, and their fluctuations occurred simultaneously with lithological changes. As
324 regards the ln-ratios within Si group of elements, such as that of K/Ti (Fig. 4e), the record
325 showed a largely antisymmetric pattern compared to that of Rb/Sr.
326 The Si-group of elements usually comprise silicate and aluminosilicate minerals, including
327 quartz, feldspars, mica, and clays. Individually, some of these elements could also correspond
328 to other groups of minerals, such as oxides (*e.g.* Al, Fe, Ti, Mn), carbonates (*e.g.* Mg, Mn), or
329 sulfides (*e.g.* Fe, Zn). However, the good correlations of these elements with Si and Al suggest
330 their dominant affiliation to aluminosilicates (Davies et al., 2015; Kylander et al.; 2011). Si
331 could also be related to biogenic sources, such as diatom frustules, formed of amorphous silica

(Peinerud, 2000), but its strong correlation with Al (Fig. 3a and 3c), which is not affected by biological processes, rules out a biogenic origin. The Si-group thus corresponds principally to the siliclastic fraction of the sediment.

Within this group, Si, Al and Ti are relatively stable and thus considered as inert elements (Wei et al., 2003). In contrast, K as well as Rb, which is associated with K, are quite mobile and could enter the lake sediment from the catchment area in mineral form (*e.g.* K-feldspars, mica or illite) or in ionic state owing the action of chemical weathering. The K/Ti ratio can therefore reflect erosional processes concerning different sources of detrital material within the watershed, but can also be an indicator of chemical weathering (Croudace and Rothwell, 2015; Xie et al., 2014). According to Xie et al. (2014), high K/Ti ratios reflect abundant K-rich minerals, especially illite, as a result of chemical weathering, whereas low K/Ti values signify low illite content but abundant Ti-rich heavy minerals. In addition, Ca-bearing carbonates and sulfates are more easily decomposed in the natural fractionation process than K-bearing minerals, so Ca-Sr minerals are leached much more readily than K-Rb minerals (Xu et al., 2010). Chemical weathering in the catchment area therefore results in lower Rb/Sr, K/Sr, Rb/Ca and K/Ca ratios in lake deposits, whereas lake sediments characterized by a higher fraction of siliclastic detritus exhibit higher values for these ratios. Based on these findings, the Rb/Sr values of lake sediments could serve as a potential indicator of the intensity of chemical weathering in the watershed, the former element decreasing while the latter increases as chemical weathering advances.

As presented in Fig. 4, K/Ti and Rb/Sr ln-ratios reflect the grain size and mineralogy of the composite core quite well. The ln(K/Ti) parameter is closely correlated with changes in the

clay and fine silt fraction of the sediment as well as with increased contents of clay minerals, namely smectite and illite (Fig. 4e, 4f, 4g). Higher values of this parameter could highlight chemical weathering within the siliclastic fraction in the catchment area. However, Kong et al. (2022) demonstrated that the fine sediments in the lake are directly related to the same material in the catchment area. The ln(K/Ti) ratio thus mainly indicates increased erosion of fine deposits from the catchment area rather than chemical weathering. High values of ln(Rb/Sr) are correlated both with increased siliclastic minerals as quartz, feldspars and mica, and with coarse grain sizes indicating erosional processes and low levels of chemical weathering (Fig. 4b, 4c, 4d). These values were recorded when ln(K/Ti) ratios were low at about 30 cal kBP and during the intervals from 20.2 to 15.2, from 13.3 to 11.8 and from 5.6 to 4.1 cal kBP. Conversely, phases corresponding to moderate and low ln(Rb/Sr) ratios (after 29.8 and up to 20.2, from 15.2 to 13.3, and between 11.8 and 5.6 cal kBP, as well as at the core top between 4.1 and 2.3 cal kBP), are thus correlated with increased chemical weathering in the catchment area; they correspond to the high ln(K/Ti) values reflecting fine-grained sediment input into the lake (Fig. 4). The major variations in ln-ratio intensities were complemented by smaller-scale changes, which will be discussed further below. These second-order changes were not evident from the mineralogical data which involved measurements at larger sampling intervals than in the case of the XRF-CS analyses.

Since chemical weathering can only occur efficiently in the presence of sufficient water, Rb/Sr ln-ratio indicate variations in water availability in the catchment area with periods of increased availability of water and hence chemical weathering when the ln(Rb/Sr) ratio is low, and periods of drought and erosion in the watershed when it is high (Fig. 4).

376 Thus, the increased ln(K/Ti) ratio, decreased ln(Rb/Sr) ratio and the corresponding deposits of
377 fine sediments at the Lake Urmia coring site are related to increased moisture levels over the
378 catchment area, whereas increased amounts of coarse clastic material were deposited during
379 drier conditions. These increased quantities of clastic material are therefore not related to a
380 generally wetter climate but rather correspond to drier conditions when the lake level was lower
381 and when more erodible material was exposed in the catchment area, as also observed in the
382 Dead Sea (Migowski et al., 2006).
383
384 5.2 The Ca-Sr group
385 Calcium and strontium intensities are highly correlated (Fig. 3a, 3d). When normalized against
386 Ti, they display similar general patterns over time, as represented by Ca/Ti ln-ratio values (Fig.
387 5a).
388 Ca is mainly present in minerals such as silicates, carbonates and sulfates, and can be associated
389 with these minerals. In lake sediments, Ca comes either from the catchment area as supplied
390 minerals or dissolved ions, or represents minerals that are chemically or biologically
391 precipitated in the lake. In Lake Urmia, Ca intensities are clearly not correlated with silicates
392 (Fig. 3), and as Ca and S intensities are only weakly correlated (Fig. 3a, 3e), Ca values also
393 reflect very little the quantity of gypsum. Consequently, Ca represents the carbonate fraction
394 and the ln(Ca/Ti) ratio could act as a proxy of the relative proportions, and hence, the relative
395 changes of carbonate and siliclastic terrigenous fluxes (Davies et al., 2015). Moreover, as
396 indicated above, Ca displays a positive linear relationship with Sr. In lake sediments, Sr can
397 originate from celestine ($SrSO_4$) but also tracks Sr-rich aragonite, which precipitates either

chemically or by biomediation in lake water, in environments characterized by high evaporation (Böning and Bard, 2009; Brisset et al., 2018). The poor correlation between S and Sr data (Fig. 3a), along with the absence of celestine in mineralogical assemblages (Kong et al. 2022), seems to confirm that Sr tracks aragonite. The correlation between Ca and Sr thus suggests that Ca is closely related to aragonite and the increase in ln(Sr/Ca) ratio may be an indicator of the presence of aragonite in the sediment. In Lake Urmia, both ln(Ca/Ti) ratio and Ca intensities without any calibration, are very closely correlated with the carbonate contents measured by Kong et al. (2022). Moreover, ln(Sr/Ca) ratios indicate the presence of aragonite previously identified as part of the calcareous mud, and more specifically present in the upper part of the core, as a component of brine shrimp fecal pellets ((Fig. 5a, 5b, 5c and 5d; Kong et al., 2022). Since the major part of the carbonate fraction is composed of aragonite, variations in the ln-ratios of Ca/Ti and Sr/Ca over time follow similar patterns.

In Lake Urmia, aragonite is mainly correlated with fine siliclastic minerals reflected by high ln(K/Ti) ratios and deposited during periods of increasing chemical weathering in the catchment area as shown by decreased ln(Rb/Sr) ratios (Fig. 4). Since its formation requires the supply of bicarbonate and Ca^{2+} through freshwater flows (Stein et al., 1997), the presence of aragonite in the lake sediments indicates a relatively humid climate. This interpretation of aragonite as an indicator of wetter conditions is specific to highly saline environments and has been proposed for the Dead Sea sediments (Stein et al., 1997). Indeed, as highlighted by Neugebauer (2016), this indication of a relatively wet environment by the presence of aragonite is generally not valid in freshwater lakes since calcite normally precipitates under humid

conditions, whereas a shift towards aragonite formation reflects drier conditions, higher salinity of the lake water and a lower lake level.

Finally, apart from aragonite, only calcite and dolomite were identified by XRD analysis, Fe, Mg and Mn carbonates being therefore absent in the sediments. Calcite and dolomite were present at relatively low contents and were either detrital or authigenic depending on their level in the sedimentary sequence (Kong et al., 2022). Their detrital contributions to the overall sediment composition are quite well expressed by the ln(Ca/Sr) ratio, showing an inverse relationship to that of the ln(Sr/Ca) ratio.

5.3. The Cl-S group

Although contributing important information on the sedimentary processes, the Cl, S and As elements composing the Cl-S group are not correlated with one another (Fig. 3a). The concentrations of Cl and S are expressed by the ln-ratios of Cl/Sr, S/Ca and Cl/S (Fig. 5e, 5f and Fig. 6b) and show less dependence on lithological changes than that of the Si and Ca-Sr groups. Arsenic is often not considered since its intensity is generally very low in lacustrine deposits and close to the detection limit of XRF analysis. However, in the Lake Urmia composite core, arsenic was detected at values clearly distinct from XRF background levels and was related to sulfur and iron mineral contents. This element will therefore be further discussed (Fig. 6b, 6c, 6d).

5.3.1. Chlorine

In saline lakes such as Lake Urmia, chlorine is mainly related to the abundance of halite in the bulk sediment and therefore reflects water salinity (Trichet et al., 2001; Brisset et al., 2021).

441 Halite was identified throughout the composite core, and semi-quantified by XRD analyses
442 (Fig. 5g). Its content could reach 10% but no trend in its evolution was detected. However,
443 detailed XRF-CS measurements clearly showed changes in chlorine content based on ln(Cl/Sr)
444 and ln(Cl/S) ratios; both strontium and sulfur may reflect the presence of evaporates in the form
445 aragonite, as discussed above, and gypsum, respectively (Fig. 5e, 5f and 6a). According to
446 these results, changes in ln(Cl/Sr) ratio largely show an antisymmetric relationship with
447 aragonite levels related to wetter conditions in the catchment area, as discussed above, and thus
448 to lower salinity of the lake water. The salinity of the lake sediments showed variations with
449 its decreased values during the following periods: (i) between about 29.8 and 20.2 cal kBP,
450 with an initially scattered signal related to changing conditions up to 22.5 cal kBP, followed
451 by more stable conditions in the second part of this interval, (ii) between 15.2 and 13.3, (iii)
452 between 11.8 and 5.6 cal, and finally, (iv) between 4.1 and 2.3 cal kBP.
453 Overall, the ln(Cl/S) ratios showed constant proportions of both elements from 30.0 up to 11.8
454 cal kBP. Notable differences were detected above this level, highlighting the relatively strong
455 decrease in Cl between 11.8 and 5.6 cal kBP (Fig. 5f).
456
457 *5.3.2. Sulfur*
458 According to Chéron et al. (2016), XRF-CS data on sulfur have been rarely reported in previous
459 studies, because of poor detection efficacy and low elemental abundance, both of which lead
460 to count rates associated with a large statistical counting error. However, in lacustrine
461 environments, XRF-CS data on sulfur have been used to identify gypsum precipitation, the
462 presence of pyrite, or soil leaching as summarized by Davis and colleagues (2015). In saline

463 lake sediments, sulfur displays quite high values and can be hosted either by sulfates (*e.g.,*
464 gypsum, anhydrite), or by sulfides (*e.g.,* pyrite, greigite). It can also occur in pore water as
465 dissolved sulfate and sulfide forms.
466
467 5.3.2.1. Calcium sulfates
468 In Dead Sea sediments, gypsum layers are reflected by the S/Ca ratio (Neugebauer et al., 2016)
469 and the presence of gypsum is interpreted as the result of mixing of the water column during
470 extremely dry years with high evaporation (Stein et al., 1997). In Lake Urmia, gypsum was the
471 only sulfate mineral identified through XRD analyses (Fig. 6a). Although the single layer of
472 gypsum was clearly in phase with an increase in sulfur content and the ln(S/Ca) ratio, this ratio
473 was only weakly correlated with gypsum (Fig. 6a, 6b). Changes in sulfur content are therefore
474 clearly dependent on another parameter and/or process.
475
476 5.3.2.2. Iron sulfides
477 Previous studies have reported the presence of both iron sulfides, namely greigite (Fe_3S_4) and
478 pyrite (FeS_2), and iron oxide, (in form of magnetite, Fe_3O_4), in Lake Urmia sediments (Tudryn
479 et al., 2021). Magnetic susceptibility provided information on these iron-bearing minerals but
480 did not permit their identification in different sections of the sediment (Fig. 6c). The presence
481 of greigite, as a magnetic mineral, is revealed by increased magnetic susceptibility when
482 present at relatively high contents. In the composite core record, peaks of magnetic
483 susceptibility were detected in organic-rich dark levels corresponding to 29.9 and at 5.5 cal
484 kBP, and between approximately 26.0 and 22.5 cal kBP, matching increases in sulfur levels

485 indicated by ln(S/Ca) ratios (Fig. 6b, 6c). When greigite is present at low concentrations or
486 when only pyrite is present, magnetic susceptibility is low, as observed between 11.8 and 5.6
487 cal kBP (Fig. 6c). Both sulfides precipitate in an anoxic, bacterial sulfate-reducing environment
488 (Berner, 1981; Curtis, 1987; Jelinowska et al., 1995; Roberts, 1995; Tudryn et al., 2010)
489 whereas magnetite is of detrital origin and indicates an oxygenated depositional environment
490 (Tudryn et al., 2021). Changes in magnetite content were recorded through both increased and
491 reduced magnetic susceptibility values in the core sections corresponding to (i) 29.8-26.0, (ii)
492 22.5-11.8, and (iii) 4.1-2.3 cal kBP (Fig. 6c). Furthermore, Tudryn et al. (2021) indicated that
493 detrital magnetite deposited between 29.8 and 26.0 cal kBP, underwent partial dissolution
494 during bacterial reduction under anoxic sediment conditions. (Fig. 6c).
495
496 5.3.2.3. Arsenic sulfides
497 Anoxic environments at the water-sediment interface or in the sediments of Lake Urmia,
498 inferred by the presence of iron sulfides and partially dissolved magnetite, coincide with
499 increased sulfur and arsenic levels (Fig. 6b, 6c, 6d).
500 Arsenic is a toxic element and its presence in sediments, groundwater and surface water results
501 from its mobilization from As-containing rocks by both natural processes and anthropogenic
502 activities. Smedley and Kinniburgh (2002) published a detailed review of As sources, behavior
503 and distribution. Mine-wastes, floodplain deposits, peat soils, lake and sea sediments can be
504 As-contaminated (Kulp et al., 2006; Le Pape et al., 2017). Since iron sulfide minerals have a
505 high capability to adsorb or co-precipitate arsenic during bacterial sulfate-reducing early
506 diagenesis in anoxic sediments or sediment-water interface, iron sulfides (pyrite, greigite)

507 represent a major host for As, and arsenic sulfides (arsenopyrite, FeAsS, realgar, As_4S_4) can
508 also precipitate (Le Pape et al., 2017; Rodriguez-Freire et al., 2016). Natural and anthropogenic
509 enrichment in arsenic, often related to iron sulfides, is known in hypersaline lakes such as Lake
510 Urmia and in sediments rich in organic matter (*e.g.,* Kulp et al., 2006; Khosravi et al., 2019).
511 The seasonally hypersaline Lake Maharlu (in southwestern Iran) receives wastewater of
512 various types produced in the basin through seasonal rivers that drain the lake's catchment area
513 (Khosravi et al., 2019). According to these authors, dissolved As concentrations at the
514 sediment–water interface are mainly controlled by evaporation, by interactions between the
515 lake water and shallow sediment pore water, and by redox processes allowing Fe and As sulfide
516 precipitation within the first centimeters of lake sediments. The hypersaline Lake Mono and
517 Lake Searles (California) contain naturally high concentrations of dissolved arsenic originating
518 from volcanic rocks (Kulp et al., 2006). These authors showed that (i) reduction can occur in
519 anoxic water and sediments, and (ii) the strongest reduction occurred in surface sediments,
520 gradually decreasing with sediment depth to undetectable levels. Anoxic conditions in organic-
521 rich environments that favor arsenic immobilization through arsenic-iron sulfides associations
522 are well known in continental and marine sediments. As-rich sulfides have been reported, for
523 example, in Holocene Mediterranean sapropel units (Thomson et al., 2006) and in the
524 Pleistocene Hetao paleolake Basin (North China) that started to shrink due to climate change
525 in the early part of the Late Pleistocene (at approximately 120 kyr) and finally became a salt
526 marsh rich in both organic matter and As-Fe sulfide associations (Wang et al., 2021).
527 In accordance with these findings, As and Fe sulfide precipitation occurs in the anoxic bottom
528 layers of the lake sediments as well as in the top layer. When present at the top of the

529 sedimentary sequence, they could be related to pollution of anthropogenic origin (Croudace et
530 al., 2019). High contents of iron sulfides and arsenic were detected in Lake Urmia sediments
531 at various depths (Fig. 6c and 6d). In addition, arsenopyrite was identified in the sample dated
532 at approximately 4.4 cal kBP in which Tudryn et al. (2021) demonstrated the presence of
533 greigite and pyrite by XRD analysis (Fig. 7). These minerals, characterized in old sediments
534 (even at around 30.0 cal kBP) are therefore of natural rather than anthropogenic origin. High
535 concentrations of As detected by XRF-CS thus indicate natural processes evidencing clear
536 anoxic conditions both (i) in lake bottom sediments during high lake levels that settled just
537 after 29.8 up to 22.0 cal kBP and from 11.8 to 5.6 cal kBP, and (ii) in organic-rich levels that
538 have been identified as reflecting the presence of salt marshes with high biological productivity
539 developing at the coring site during low stands of the lake at approximately 30.0-29.8 and 5.5
540 cal kBP (Tudryn et al., 2021).
541
542 **6. Discussion**
543
544 Lake Urmia is mainly controlled by the precipitation-evaporation balance in its catchment area.
545 The main markers of the precipitation-evaporation rates at the coring site and hence the water
546 salinity and lake level are (i) the siliclastic fraction, which is an expression of the transfer of
547 detrital material from the catchment area into the lake under wet or dry conditions, and (ii) the
548 authigenic fraction (carbonate, gypsum and halite), which is directly related to the ionic
549 concentrations in the lake water. In addition, iron and arsenic sulfides are good indicators of
550 anoxic conditions both in the sediment and at the water-sediment interface. XRF-CS elemental

551 data integrate full information concerning these minerals. Previous studies on both grain size
552 and the major mineralogical phases (Tudryn et al., 2021; Kong et al., 2022) allowed precise
553 calibration of these XRF-CS elemental data in terms of the relative abundances of each element,
554 as well as identification of their environmental significance as regards the physical and
555 geochemical processes occurring in the catchment area and in the lake. Since XRF-CS analyses
556 were performed every 5 mm of the sediment core, and not at every 5 cm or at even greater
557 intervals as was the case in mineralogical studies (Kong et al., 2022), a detailed environmental
558 record was obtained. Humid conditions and high lake stands were highlighted in lake sediments
559 by (i) low ln(Rb/Sr) ratios and high ln(Ca/Ti) ratios, both indicating the predominance of
560 chemical weathering in the catchment area, (ii) high ln(K/Ti) ratios indicating the deposition
561 of fine-grained siliclastic minerals, mainly clays, (iii) high values of ln(Sr/Ca) ratios, reflecting
562 carbonate precipitation in the lake water, mainly in the form of aragonite, (iv) low values of
563 ln(Cl/Sr) ratios fingerprinting decreased water salinity, and (v) predominantly anoxic
564 depositional conditions with precipitation of iron and arsenic sulfides under anoxic, sulfate-
565 reducing bottom conditions shown by increasing As intensities on XRF-CS record. The
566 inversion of the ln-ratio values specified above, showed erosion in the catchment area and
567 deposit of coarse-grained silicates (quartz, feldspars and mica) and detrital carbonates (calcite,
568 dolomite) at the coring site, in a well-oxygenated environment with increased salinity. These
569 characteristics indicate generally dry conditions, a low lake level and an influence of the river
570 at the core site. Anoxic conditions predominated only during two low stands characterized by
571 high organic contents.
572

573 6.1. Lake Urmia over the last 30 cal kBP

574 The results of previous palynonogical studies suggested a high lake water level during the last
575 glacial period as a whole (Djamali et al., 2008a). On the basis of stable isotope analyses,
576 Stevens et al. (2012) described dry conditions during the Late Pleistocene with a short-lived
577 lacustrine episode at ~14 kyr, followed by a drying out period probably in phase with the
578 Younger Dryas, with no re-establishment of lacustrine conditions until ~ 10 kyr. Kelts and
579 Shahrabi (1986) identified three lacustrine high stands and two low stands during the Holocene,
580 based on sedimentological data. However, they highlighted the lack of readily dateable material
581 in their study. They nevertheless proposed that one of the identified high lake stands could have
582 occurred at approximately 9–7.5 kyr BP. The data presented in this paper provide a detailed
583 record of the evolution of Lake Urmia during the Late Pleistocene, including LGM and the
584 Late Glacial period, as well as during the Holocene.

585

586 *Late Pleistocene*

587 *Between around 30.00 and 29.8 cal kBP*, the presence of sandy and silty detrital siliclastic
588 minerals suggest the direct influence of the Shahr Chay River, with no or very shallow lake
589 water at the coring site and possible development of salt marshes (Tudryn et al., 2021; Kong et
590 al., 2022). The black and dark-gray sediment highlights the presence of an organic fraction, as
591 well as the iron sulfides (greigite and pyrite) that have been previously identified (Tudryn et
592 al., 2021) and arsenic sulfides determined on the basis of XRF-As data. All these sediment
593 components indicate anoxic depositional conditions. Erosional processes in the catchment area
594 are evidenced by high values of ln(Rb/Sr) and low values of ln(Ca/Ti). Moreover, high ln(Cl/Sr)

595 values indicate a highly saline environment at the coring site. Such erosional processes and
596 saline environments reflect generally dry conditions, with low water availability in the
597 catchment area and a low stand of the lake.
598 *Between* 29.8 and *20.2 cal kyr BP*, the lacustrine conditions established at the coring site
599 resulted in gray, homogeneous sediments dominated by fine silts and clays. Detrital silicates
600 are mainly represented by quartz, mica, feldspars and clays (mostly smectite and illite).
601 Carbonaceous mud is dominated by authigenic aragonite, totally absent from the under lying
602 sediment, as well as by detrital calcite and dolomite of both authigenic and detrital origins
603 (Kong et al., 2022). Crystallization of aragonite and dolomite requires a high Mg^{2+} content in
604 water to become the stable species of calcium and magnesium carbonates, thereby indicating
605 high evaporative conditions in agreement with the presence of halite, which was also identified.
606 As suggested by Kong et al. (2022), the presence of few or no fecal pellets of *Artemia urmiana*
607 shrimps may indicate that the lake water was too cold for their development. This result seems
608 to be consistent with the cold climate of this period belonging to the LGM.
609 XRF-CS data showing low values of ln(Rb/Sr), as well as high values of ln(Ca/Ti) and
610 ln(Sr/Ca), emphasize the importance of chemical weathering of sediments in the catchment
611 area and precipitation of carbonates in the lake (Figs. 4 and 5). Furthermore, the increased
612 ln(K/Ti) values reflect the erosion and transport into the lake of a fine grained siliclastic fraction.
613 Such an overall pattern indicates humid conditions during the LGM time as a whole, a relatively
614 low salinity of the lake water expressed by low ln(Cl/Sr) values, which still remained salty, and
615 a high lake level (Fig. 5). Moreover, the magnetic and As-XRF-CS data indicate anoxic bottom

616 conditions up to around 22.5 cal kBP, which then evolve into a well-oxygenated environment
617 (Fig. 6).
618 The general pattern of wet and cold conditions in the catchment area and the high water level
619 is complemented by the short-term changes revealed by the CS-XRF data thanks to the high
620 measurement step. With regard to the 30.0 and 24.0 cal kBP period, these spells could be clearly
621 distinguished, as shown in Fig. 8a with regard to the ln(Ca/Ti) profile. During the 28.6-28.3
622 and 27.3-27.1 cal kBP intervals, ln(Ca/Ti) and ln(Sr/Ca) values increased simultaneously with
623 the decreases in ln(Rb/Sr) and ln(Cl/Sr) values. This indicates enhanced chemical weathering
624 in the catchment area due to a high moisture level and the precipitation of authigenic carbonates
625 in the lake, as well as reduced water salinity implying an increase in the water level of the lake.
626 In addition, the following four intervals: (i) 27.0-26.8, (ii) 26.3-26.0, (iii) 25.6-25.3 and (iv)
627 24.6-24.4 cal kBP show an inverse pattern of these parameters indicating overall drying
628 conditions in the catchment area. Each of these events occurs over a very short period of time,
629 at most 300 years, but each short period nevertheless shows internal variations indicating even
630 more rapid changes. For example, the globally drier period between 24.6 and 24.4 cal kBP,
631 includes three matched dry-wet sequences corresponding to changes on a scale of less than 50
632 years.
633 *Between 20.2 cal kBP and 11.8 cal kBP*, sediments at the coring site are mainly composed of
634 coarse-grained detrital silicates and some detrital carbonates having been deposited in a well-
635 oxygenated environment (Fig. 6). High values of ln(Rb/Sr) and ln(Cl/Sr), as well as low values
636 of ln(Ca/Ti) and ln(Sr/Ca) indicate increased erosion over the catchment area with a suspended
637 load brought by the Shahr Chay River at the coring site and high saline depositional conditions.

638 All these parameters show dry conditions in the lake catchment area and a low lake level.
639 However, this dry interval was evidently interrupted by an increase in moisture level and the
640 establishment of a clearly lacustrine environment at the coring site between 15.2 and 13.3 cal
641 kBP, with increased fine grained detrital input into the lake, precipitation of carbonates in the
642 lake water and less evaporative conditions than those apparent just before and after, but in a
643 still well-ventilated basin (Kong et al., 2022). This high humidity spell is expressed by
644 decreased ln(Rb/Sr) and ln(Cl/Sr) values and increased ln(K/Ti), ln(Ca/Ti) and ln(Sr/Ca) values
645 and shows a timing in good agreement with the Bølling–Allerød warming during the late
646 glacial period. The return to a regressive stage of the lake between 13.3 and 11.8 cal kBP
647 corresponds to the Younger Dryas cooling before the Holocene (Fig. 8).
648
649 *Holocene*
650 *The 11.8-5.6 cal kBP interval* is characterized by humid conditions and the re-establishment of
651 an evidently lacustrine environment at the coring site. High chemical weathering in the
652 catchment area, precipitation of carbonate in the lake and a relatively low salinity are indicated
653 through low values of ln(Rb/Sr) and ln(Cl/Sr), and high values of ln(Ca/Ti) and ln(Sr/Ca) (Fig.
654 4 and 5). Sediments are composed of fine-grained particles with very low contents of detrital
655 minerals and of authigenic carbonates, mostly aragonite in the form of shrimp fecal pellets that
656 form the dominant component of the sediment (Kong et al., 2022). Furthermore, the
657 concentration of shrimp fecal pellets that appear for the first time in such impressive quantities
658 in this interval, is linked to a specific range of water salinity (100 and 300 $g.L^{-1}$), as well as to
659 other parameters, including temperature that create favorable conditions for shrimp

development (Wurtsbaugh and Gliwicz, 2001; Agh et al., 2008; Esmaeili Dahesht et al., 2010; Sharifi et al., 2018). The middle part of this sequence, at about 8 cal kBP is less well represented in core data but all parameters suggest the decrease in available moisture in the catchment area. The presence of some iron sulfides (Tudryn et al., 2021) and arsenic sulfides throughout this interval suggests poor bottom water ventilation.

The 5.6–4.1 cal kyr BP interval is characterized by high ln(Rb/Sr) and ln(Cl/Sr) values and low ln(Ca/Ti) and ln(Ca/Sr) values, as well as by a sediment composed of sandy and silty detrital silicates and few detrital carbonates. These parameters, as at around 30 cal kBP, are in good agreement with low moisture levels in the catchment area, the only influence of the Shahr Chay River at the coring site with no or very shallow water and thus overall a low lake level (Fig. 6). The lower part of this section at about 5.5 cal kBP is rich in vegetation remains, as at 30 cal kBP. At both these core levels, rich in organic remains, iron and arsenic sulfides are particularly abundant indicating an anoxic environment. Nevertheless, in contrast to the core bottom, where the charcoals exhibit $\delta^{13}C$ values of C3 plants (26.5 and 25.5 ‰ vs V-PDB; Deines, 1980), charcoal samples at this 5.5 cal kBP level display the same $\delta^{13}C$ values as well as values of 13.5 and 14.5 ‰ vs V-PDB, indicating the coexistence of both C3 and C4 vegetation types on the watershed at the time of deposition (Tudryn et al., 2021; Kong et al., 2022). The C4 and C3 vegetation episode lasted from 5.6 to 4.1 cal kyr BP, and likely indicates a warmer and drier episode than that occurring at 30 cal kyr BP.

In the last recorded interval 4.1–2.3 cal kBP, low ln(Rb/Sr) and ln(Cl/Sr) values and high ln(Ca/Ti) and ln(Ca/Sr) values indicate the return to moist conditions and a higher lake level with chemical weathering in the catchment area and carbonate precipitation in the lake water

682 at the coring site. Authigenic carbonates are mainly composed of shrimp fecal pellets indicating
683 an adequate water salinity range for shrimp development (Wurtsbaugh and Gliwicz, 2001; Agh
684 et al., 2008; Esmaeili Dahesht et al., 2010; Sharifi et al., 2018). The predominant sandy and
685 silty fraction reflects a high energy transport from the Shahr Chay River, while the presence of
686 magnetic oxides indicates well oxygenated depositional conditions.
687 The general context of wet conditions in the catchment area and high lake level can be
688 completed by the short-term variations observed in parameters such as ln(Ca/Ti) (Fig. 8a).
689 During the 4.1-3.6 and 3.4-3.3cal kBP intervals, this parameter varies abruptly, indicating
690 unstable moisture conditions for about 500 and 100-200 years respectively, with lower
691 available moisture from 3.6 to 3.4 cal kBP. Thereafter, ln(Ca/Ti) values are gradually enhanced
692 up to 2.3 cal kBP indicating increasingly humid conditions.
693
694 6.2. Lake Urmia and the regional scale
695 Progression from the lake basin scale to larger scale of the eastern Mediterranean and western
696 Asia region as a whole, the data from Lake Urmia fill an important gap in paleoclimatic records,
697 providing a continuous record with very good temporal resolution that can be compared to
698 other regional records. Existing lake records are often discontinuous or very short, or on very
699 long time scales with relatively low resolutions, and include Lake Urmia (Djamali et al., 2008a;
700 Djamali et al., 2008b; Kelts and Shahrabi, 1986; Stevens et al., 2012; Talebi et al., 2016), Lakes
701 Zeribar, Mirabad and Neor, the areas respectively south and north of Lake Urmia in Iran
702 (Wasylikowa et al., 2006; Stevens et al., 2006; Sharifi et al., 2015), Anatolian lakes such as
703 Konya Plain, Gölhisar, Eski Acigöl, Nar, Burdur, as well as the Dead Sea (Fontugne et al.,

1999; Roberts et al., 2001, 2008; Bartov et al., 2003; Jones et al., 2006, 2007; Kuzucuoğlu et al., 2010; Turner et al., 2008; Stein et al., 2010; Tudryn et al., 2013; Ön et al., 2018) (Fig. 1a). More detailed XRF-CS data covering the last 30 cal kBP, are available for Lake Van and for the Black Sea, both located close to Lake Urmia, and covering 17.5 cal kBP from Lake Hazar in south-eastern Anatolia (Fig. 8). In Lake Van, the two independent Ca/K and Ca/Fe records reveal a close relationship between authigenic carbonate precipitation and siliciclastic material input from the drainage basin (Çağatay et al., 2014; Kwiecien et al., 2014). In Lake Hazar, the XRF-Ca record represents a chemically or biologically precipitated calcium carbonate (Ön et al., 2018). In the Black Sea sediments, the XRF-Ca profile reflects the variability of productivity of Black Sea "Lake" surface waters (Bahr et al., 2005; Constantinescu et al., 2015; Kwiecien et al., 2009; Major et al., 2002; Soulet et al., 2011). Despite the high temporal resolution of these data, the short-term changes identified in Lake Urmia between 28.6 and 24.4 cal kBP, are not observed at all (Fig. 8). Since the Black Sea depositional system integrates a very large catchment area encompassing various geographical and climatic zones, it was certainly not sufficiently sensitive to differentiate the moderate amplitude of these short-term fluctuations. In contrast, "amplification-type" lakes, *i.e.*, closed, smaller-sized lakes, are very sensitive to the conditions in their catchment area reflecting both local and regional variations, and their water balance is essentially and/or directly linked to climatic fluctuations. In addition, sedimentation rates are often high and even small, short-term variations can therefore be detected more easily than in the marine environment. In the deep, endorheic Lake Van, however, some changes may be observed in the Ca/K and Ca/Fe records, but it is still not evident to clearly distinguish the same six short-time episodes between 29 and 24 cal kBP as

726 those discerned with regard to Lake Urmia (Fig. 8). This might be due to a lower temporal
727 resolution of the Lake Van data compared to that archived for Lake Urmia or rather to the fact
728 that in the shallow Lake Urmia even small changes stand out more clearly. These short-lived
729 events recorded at Lake Urmia occurred during a period that in any case was wet in the east
730 Mediterranean and west Asian areas as evidenced by high water levels in the Caspian Sea,
731 Lakes Zeribar, Van, the Konya Plain, and the Dead Sea (Fontugne et al., 1999; Kuzucuoglu et
732 al., 1999, 2010; Bartov et al., 2003; Bookman et al., 2004; Wasylikowa et al., 2006; Çağatay
733 et al., 2014; Kwiecien et al., 2014; Tudryn et al., 2022). The two peaks at 28.6-28.3 and 27.3-
734 27.1 cal kBP related to increased moisture in the Lake Urmia catchment area, coincide with
735 the two $\delta^{18}O$ peaks recorded in the North Greenland ice core (North Greenland Ice Core Project
736 (NGRIP) Members, 2004) reflecting rapid warming episodes in the Northern Hemisphere, the
737 so-called "Dansgaard–Oeschger" (D-O) events 4 and 3 (Fig. 8). In contrast, four drier episodes
738 at Lake Urmia at 27.0-26.8, 26.3-26.0, 25.6-25.3 and 24.6-24.4 cal kBP, appear to be unrelated
739 to changes recorded in the NGRIP curve and therefore may reflect local conditions. However,
740 their timing corresponds to the first stage of the LGM and could reflect increased aridity in
741 Lake Urmia area before recovering of more stable and humid conditions between 22.5 and 20.2
742 cal kBP (Fig. 8).
743 The larger and contrasted climate changes occurring after the LGM are clearly reflected in all
744 XRF data from Lakes Urmia, Hazar, Van, as well as from the Black Sea, and are in agreement
745 with the Northern Hemisphere NGRIP climate records (Fig. 8). Indeed, the warm and wet
746 Bølling–Allerød and Early Holocene oscillations are very clearly differentiated by the
747 geochemically remarkable maxima in Ca/Ti-, Ca/K-, Ca/Fe-ratios and XRF-Ca intensities,

748 with the exception for Bølling–Allerød warming in Lake Hazar record (Fig. 8; Bahr et al., 2005;
749 Kwiecien et al., 2009, 2014; Major et al., 2002; Soulet et al., 2011; Çağatay et al., 2014). These
750 episodes correspond to a rise in lake water levels during the Bølling–Allerød oscillation (Lakes
751 Urmia, Van, Zeribar, Konya Plain and Hazar, as well as the Dead Sea) and to the lacustrine
752 environment (Lakes Urmia, Van Zeribar, Hazar, Gölhisar) or at least, to the establishment of
753 marshes (Konya Plain) during the Early-Mid Holocene (Fontugne et al., 1999; Kuzucuoglu et
754 al., 1999, 2010; Wasylikowa et al., 2006; Eastwood et al., 2007 Stevens et al., 2001, 2012;
755 Çağatay et al., 2014; Ön et al., 2018). The Late Holocene appears to coincide with greater
756 contrasts within the east Mediterranean and west Asia region with the persistence of open lakes
757 in the eastern part (Lakes Van, Urmia, Hazar, Zeribar) and a decrease in their level or even a
758 total drying up in the western part (Konya Plain, Gölhisar, Dead Sea) (Bartov et al., 2003;
759 Fontugne et al., 1999; Kuzucuoglu et al., 1999, 2010; Wasylikowa et al., 2006; Eastwood et
760 al., 2007; Çağatay et al., 2014; Ön et al., 2018). Low XRF values of Ca/Ti, Ca/K-, Ca/Fe-ratios
761 and low XRF-Ca intensities indicate increased detrital input, a dry climate and evaporative
762 regression of Lake Urmia and Lake Van levels, as well as low productivity of the Black Sea.
763 These results are consistent with a general decrease in level or drying up of lakes in the region
764 during the Younger Dryas cooling, and during the Holocene Rapid Climate Changes (RCCs)
765 recorded in the Northern Hemisphere as a decrease in temperature between 9 and 8 cal kBP
766 (8.2 kBP on the NGRIP curve; Fig. 8), and as cooling at high latitudes and increased
767 aridification at low latitudes in the Mid-Holocene (Mayewski et al., 2004). The Mid-Holocene
768 lakes in the eastern Mediterranean and western Asia region generally decreased in level and
769 even dried up. This was probably linked to the drought recorded at 5.2 cal kyr BP and evidenced

770 in the speleothem record of the Soreq Cave (Bar-Matthews et al., 1997), as well as those
771 recorded around 5.2 and 4.2 cal kyr BP in many sites throughout the eastern Mediterranean
772 area and Asia (Staubwasser and Weiss, 2006). The re-establishment of wetter but changing
773 conditions in the Lake Urmia catchment is indicated by the increase in the Ca/Ti ratio during
774 (i) 4.1-3.6 and (ii) 3.4-3.3 cal kBP and its fall in between. These variations are in agreement
775 with those of Lake Hazar (Fig. 8b, c).
776 The climate change recorded at Lake Urmia as well as in the eastern Mediterranean and western
777 Asia region in general, shows an overall homogeneity with the changes recorded in the North
778 Greenland ice cores over the last 30 millennia (Fig. 8f). This emphasizes the major influence
779 of the North Atlantic climate system, even with respect to very short-term changes, on this
780 region as it is today. The trajectories and magnitude of the moist air masses coming from the
781 North Atlantic and the Mediterranean, carried by the westerlies in winter and spring are
782 controlled by the climatic variability in the North Atlantic and by the strength of the cold, dry
783 northeasterly winds coming from the Siberian high (Alijani and Harman, 1985; Stevens et al.,
784 2001; Kehl, 2009; Akçar et Schlüchter, 2005). In summer, the subtropical high-pressure belt
785 spreads over nearly the whole of Iran, resulting in northeasterly winds generating hot, dry
786 conditions (Stappen et al., 2001). However, moisture distribution is more complicated than this
787 general pattern, as available data indicate that during the Holocene, moisture was less available
788 in Inner Anatolia than further east on the Turkish-Iranian plateau where Lakes Urmia and Van
789 are located. Djamali et al. (2010) also highlighted the discrepancy between the increased
790 moisture levels indicated by the rise in lake water levels at the beginning of the Holocene and
791 the postglacial expansion on deciduous oak woodlands of the Zagros - Anti-Taurus Mountains,

792 which was delayed until the mid-Holocene at around 6300 cal. yr BP. To explain this
793 discrepancy, these authors suggested a different seasonality of precipitation during the early
794 Holocene compared to the late Holocene; the intensification of the Indian summer monsoon
795 during the early Holocene could have reduced or eliminated the spring rainfall in
796 western/northwestern Iran and eastern Anatolia, which in turn may have delayed the
797 development of the Zagros - Anti-Taurus woodlands.
798
799 7. Conclusion
800
801 The results of the XRF elemental analyses of Lake Urmia sediments, in combination with
802 mineralogy, magnetic susceptibility and other sedimentological records, constitute a
803 continuous 30 cal kBP record of the lake's evolution, encompassing several environmental
804 phases as follows:
805 1- periods of increasing chemical weathering in the catchment area in conjunction with fine
806 grain deposition and carbonate precipitation in the lake reflecting both wet conditions
807 associated with high lake levels and lower salinity were identified at the following intervals: (i)
808 29.8-20.2, (ii) 15.2-13.3, (iii) 11.8-5.6 and (iv) 4.1-2.3 cal kBP.
809 2- stages of increasing erosion in the lake catchment area, linked to siliclastic deposits in the
810 lake during drier conditions and lower lake levels with higher salinity were detected at around
811 30-29.8 cal kBP, as well as between 20.2 and 15.2, between 13.3 and 11.8, and between 5.6
812 and 4.1 cal kBP.

3- short-lived increases in chemical weathering in the catchment area during the following intervals: (i) 28.6-28.3, (ii) 27.3-27.1, (iii) 4.1-3.6 and (iv) 3.4-3.3 cal kBP as well as four intervals of increasing erosion at (i) 27.0-26.8, (ii) 26.3-26.0, (iii) 25.6-25.3 and (iv) 24.6-24.4 cal kBP.

Superimposed on these results, XRF data on Lake Urmia deposits revealed the presence of arsenic of natural origin at concentrations above background levels at the lake-sediment interface or in the first centimeters of sediments. Arsenic appears to be systematically associated with iron sulfides, both being of early diagenetic origin, and indicating anoxic conditions in (i) lake bottom sediments during high lake water levels after 29.8 and up to 22.0 cal kBP and from 11.8 to 5.6 cal kBP, and (ii) levels rich in organic matter during low stands of the at 29.9 and 5.5 cal kBP.

On a more global scale, our results concerning the reconstruction of the environmental phases of Lake Urmia fit well into the evolution of the eastern Mediterranean and western Asian regions, especially during the wet and dry spells corresponding to the Bølling–Allerød and Younger Dryas oscillations respectively, as well as during the LGM and the Holocene. A very good correlation of these changes, and even of those of short duration with the North Atlantic climate system such as the D-O 4 and D-O 3 events, clearly indicates that the region has been influenced predominantly by this system during the last 30 kBP.

Declaration of competing interest

834 The authors declare that they have no known competing financial interests or personal
835 relationships that could have appeared to influence the work reported in this paper.
836
837 Acknowledgement
838
839 This work was supported by the French-Iranian project Gundishapur, the Center for
840 International Scientific Studies and Collaboration (CISSC, Iran), TelluS Program of
841 CNRS/INSU and China Scholarship Council (CSC). We are very grateful to Aline Govin
842 (Laboratoire des Sciences du Climat et de l'Environnement, CEA-CNRS-UVSQ, France) for
843 fruitful discussions. The anonymous reviewers are thanked for their suggestions and comments,
844 which helped to improve the manuscript.
845
846 References
847
848 Agh, N., Van Stappen, G., Bossier, P., Sepehri, H., Lotfi, V., Rouhani, S., Sorgeloos, P., 2008.
849 Effects of salinity on survival, growth, reproductive and life span characteristics of
850 Artemia populations from Urmia Lake and neighboring lagoons. Pakistan journal of
851 biological sciences: PJBS 11, 164-172.
852 Ahmady-Birgani, H., Ravan, P., Schlosser, J.S., Cuevas-Robles, A., AzadiAghdam, M.,
853 Sorooshian, A., 2020. On the chemical nature of wet deposition over a major desiccated
854 lake: Case study for Lake Urmia basin. Atmospheric Research 234, 104762.

855 Akçar, N., Schlüchter, C., 2005. Paleoglaciations in Anatolia: a schematic review and first
856 results. Eiszeitalter und Gegenwart E&G/Quaternary science journal 55, 102-121.
857 Alijani, B., Harman, J.R., 1985. Synoptic climatology of precipitation in Iran. Annals of the
858 Association of American Geographers 75, 404-416.
859 Alipour, S., 2006. Hydrogeochemistry of seasonal variation of Urmia Salt Lake, Iran. Saline
860 systems 2, 1-19
861 Allen, M., Saville, C., Blanc, E.P., Talebian, M., Nissen, E., 2013. Orogenic plateau growth:
862 Expansion of the Turkish-Iranian Plateau across the Zagros fold-and-thrust belt. Tectonics
863 32, 171-190.
864 Asem, A., Eimanifar, A., van Stappen, G., Sun, S.C., 2019. The impact of one-decade
865 ecological disturbance on genetic changes: a study on the brine shrimp Artemia urmiana
866 from Urmia Lake, Iran. Peerj 7.
867 Bahr, A., Lamy, F., Arz, H., Kuhlmann, H., Wefer, G., 2005. Late glacial to Holocene climate
868 and sedimentation history in the NW Black Sea. Marine Geology 214, 309-322.
869 Bar-Matthews, M., Ayalon, A., Kaufman, A., 1997. Late Quaternary paleoclimate in the
870 eastern Mediterranean region from stable isotope analysis of speleothems at Soreq Cave,
871 Israel. Quaternary Research 47, 155-168.
872 Bartov, Y., Goldstein, S.L., Stein, M., Enzel, Y., 2003. Catastrophic arid episodes in the
873 Eastern Mediterranean linked with the North Atlantic Heinrich events. Geology 31, 439-
874 442.
875 Berberian, M., Arshadi, S., 1976. On the evidence of the youngest activity of the North Tabriz
876 Fault and the seismicity of Tabriz city. Geol. Surv. Iran Rep 39, 397-418.

877 Berner, R.A., 1981. A new geochemical classification of sedimentary environments. Journal
878 of Sedimentary Research 51, 359-365.
879 Bookman (Ken-Tor), R., Enzel, Y., Agnon, A., Stein, M., 2004. Late Holocene lake levels of
880 the Dead Sea. Geological Society of America Bulletin 116, 555-571.
881 Bottema, S., 1986. A Late quaternary pollen diagram from Lake Urmia (Northwestern Iran).
882 Review of Palaeobotany and Palynology 47, 241-261
883 Böning, P., Bard, E., 2009. Millennial/centennial-scale thermocline ventilation changes in the
884 Indian Ocean as reflected by aragonite preservation and geochemical variations in Arabian
885 Sea sediments. Geochimica et Cosmochimica Acta 73, 6771-6788.
886 Brisset, E., Djamali, M., Bard, E., Borschneck, D., Gandouin, E., Garcia, M., Stevens, L.,
887 Tachikawa, K., 2018. Late Holocene hydrology of Lake Maharlou, southwest Iran,
888 inferred from high-resolution sedimentological and geochemical analyses. Journal of
889 Paleolimnology 61, 111-128.
890 Çağatay, M.N., Öğretmen, N., Damcı, E., Stockhecke, M., Sancar, Ü., Eriş, K.K., Özeren, S.,
891 2014. Lake level and climate records of the last 90ka from the Northern Basin of Lake
892 Van, eastern Turkey. Quaternary Science Reviews 104, 97-116.
893 Chaudhari, S., Felfelani, F., Shin, S., Pokhrel, Y., 2018. Climate and anthropogenic
894 contributions to the desiccation of the second largest saline lake in the twentieth century.
895 Journal of Hydrology 560, 342-353.
896 Chéron, S., Etoubleau, J., Bayon, G., Garziglia, S. and Boissier, A., 2016. Focus on sulfur count
897 rates along marine sediment cores acquired by XRF Core Scanner. X-Ray Spectrometry
898 45, 288-298.

899 Constantinescu, A., Toucanne, S., Dennielou, B., Jorry, S., Mulder, T., Lericolais, 2015.
900 Evolution of the Danube deep-sea fan since the last glacial maximum: new insights into
901 Black Sea water-level fluctuations. Marine Geology 367, 50-68.
902 Croudace, I.W. and Rothwell, R.G., 2015. Micro-XRF Studies of Sediment Cores:
903 Applications of a non-destructive tool for the environmental sciences, 17. Springer.
904 Croudace, I.W., Teasdale, P.A., Cundy, A.B., 2019. 200-year industrial archaeological record
905 preserved in an Isle of Man saltmarsh sediment sequence: Geochemical and
906 radiochronological evidence. Quaternary International 514, 195-203.
907 Curtis, C., 1987. Mineralogical consequences of organic matter degradation in sediments:
908 inorganic/organic diagenesis, Marine clastic sedimentology. Springer, pp. 108-123.
909 Danesh-Yazdi, M., Ataie-Ashtiani, B., 2019. Lake Urmia crisis and restoration plan: Planning
910 without appropriate data and model is gambling. Journal of Hydrology 576, 639-651.
911 Davies, S.J., Lamb, H.F., Roberts, S.J., 2015. Micro-XRF Core Scanning in Palaeolimnology:
912 Recent Developments, Micro-XRF Studies of Sediment Cores. Developments in
913 Paleoenvironmental Research, pp. 189-226.
914 Deines, P., 1980. The isotopic composition of reduced organic carbon. In P. Fritz & J.C. Fontes
915 (eds.), Handbook of environmental isotope geochemistry. Elsevier, Amsterdam, New
916 York, 329-406.
917 Djamali, M., de Beaulieu, J.-L., Shah-hosseini, M., Andrieu-Ponel, V., Ponel, P., Amini, A.,
918 Akhani, H., Leroy, S.A.G., Stevens, L., Lahijani, H., Brewer, S., 2008a. A late Pleistocene
919 long pollen record from Lake Urmia, Nw Iran. Quaternary Research 69, 413-420.

Djamali, M., Kürschner, H., Akhani, H., de Beaulieu, J.L., Amini, A., Andrieu-Ponel, V., Ponel, P., Stevens, L., 2008b. Palaeoecological significance of the spores of the liverwort Riella (Riellaceae) in a late Pleistocene long pollen record from the hypersaline Lake Urmia, NW Iran. Review of Palaeobotany and Palynology 152, 66-73.

Djamali, M., Akhani, H., Andrieu-Ponel, V., Braconnot, P., Brewer, S., de Beaulieu, J.L., Fleitmann, D., Fleury, J., Gasse, F., Guibal, F., Jackson, T., Lézine, A.M., Médail, F., Ponel, P., Roberts, N., Stevens, L., 2010. Indian Summer Monsoon variations could have affected the early-Holocene woodland expansion in the Near East, The Holocene, 20(5), 813-820.

Eastwood, W.J., Leng, M.J., Roberts, N., Davis, B., 2007. Holocene climate change in the eastern Mediterranean region: a comparison of stable isotope and pollen data from Lake Gölhisar, southwest Turkey. Journal of Quaternary Science 22, 327-341.

Eimanifar, A. and Mohebbi, F., 2007. Urmia Lake (Northwest Iran): a brief review. Saline Systems 3, 1-8.

Esmaeili Dahesht, L., Negarestan, H., Eimanifar, A., Mohebbi, F., Ahmadi, R., 2010. The fluctuations of physicochemical factors and phytoplankton populations of Urmia Lake, Iran. Iranian Journal of Fisheries Sciences 9, 361-381.

Evans, G., Augustinus, P., Gadd, P., Zawadzki, A., Ditchfield, A., 2019. A multi-proxy μ-XRF inferred lake sediment record of environmental change spanning the last ca. 2230 years from Lake Kanono, Northland, New Zealand. Quaternary Science Reviews 225, 106000.

940 Finné, M., Holmgren, K., Sundqvist, H.S., Weiberg, E., Lindblom, M., 2011. Climate in the
941 eastern Mediterranean, and adjacent regions, during the past 6000 years–A review.
942 Journal of archaeological science 38, 3153-3173.
943 Fontugne, M., Kuzucuoğlu, C., Karabiyikoğlu, M., Hatte, C., Pastre, J.F., 1999. From
944 Pleniglacial to Holocene: a 14C chronostratigraphy of environmental changes in the
945 Konya Plain, Turkey. Quaternary Science Reviews 18, 573-591.
946 Guo, F., Clemens, S., Liu, X., Long, Y., Li, D., Tan, L., Liu, C., Yan, H., Sun, Y., 2021.
947 Application of XRF scanning to different geological archives. Earth and Space Science 8,
948 e2020EA001589.
949 Hennekam, R., Sweere, T., Tjallingii, R., de Lange, G.J., Reichart, G.-J., 2019. Trace metal
950 analysis of sediment cores using a novel X-ray fluorescence core scanning method.
951 Quaternary International 514, 55-67.
952 Jalili, S., Kirchner, I., Livingstone, D.M., Morid, S., 2012. The influence of large-scale
953 atmospheric circulation weather types on variations in the water level of Lake Urmia, Iran.
954 International Journal of Climatology 32, 1990-1996.
955 Jelinowska, A., Tucholka, P., Gasse, F., Fontes, J.-C., 1995. Mineral magnetic record of
956 environment in late Pleistocene and Holocene sediments, Lake Manas, Xinjiang, China.
957 Geophysical Research Letters 22, 953-956.
958 Jones, M.D., Roberts, C.N., Leng, M.J., 2007. Quantifying climatic change through the last
959 glacial–interglacial transition based on lake isotope palaeohydrology from central Turkey.
960 Quaternary Research 67, 463-473.

961 Jones, M.D., Roberts, C.N., Leng, M.J., Türkeş, M., 2006. A high-resolution late Holocene
962 lake isotope record from Turkey and links to North Atlantic and monsoon climate.
963 Geology 34, 361-364.
964 Kehl, M., 2009. Quaternary climate change in Iran - the state of knowledge. Erdkunde 63, 1-
965 17.
966 Kelts, K., Shahrabi, M., 1986. Holocene sedimentology of hypersaline Lake Urmia,
967 northwestern Iran. Palaeogeography, Palaeoclimatology, Palaeoecology 54, 105-130.
968 Khazaei, B., Khatami, S., Alemohammad, S.H., Rashidi, L., Wu, C., Madani, K., Kalantari, Z.,
969 Destouni, G., Aghakouchak, A., 2019. Climatic or regionally induced by humans? Tracing
970 hydro-climatic and land-use changes to better understand the Lake Urmia tragedy. Journal
971 of Hydrology 569, 203-217.
972 Khosravi, R., Zarei, M., Sracek, O., Bigalke, M., 2019. Geochemical and hydrological controls
973 of arsenic concentrations across the sediment–water interface at Maharlu Lake, Southern
974 Iran. Applied geochemistry 102, 88-101.
975 Kong, T., Tudryn, A., Gibert-Brunet, E., Tucholka, P., Motavalli-Anbaran, S-H., Ahmady-
976 Birgani, H., Lankarani, M., Miska, S., Noret, A., Dufaure, O., 2022. 30,000 years of the
977 southwestern Lake Urmia (Iran) evolution inferred from mineralogical indicators, Journal
978 of Asian Earth Sciences 239, 105387.
979 Kulp, T., Hoeft, S., Miller, L., Saltikov, C., Murphy, J., Han, S., Lanoil, B., Oremland, R., 2006.
980 Dissimilatory arsenate and sulfate reduction in sediments of two hypersaline, arsenic-rich
981 soda lakes: Mono and Searles Lakes, California. Applied and environmental microbiology
982 72, 6514-6526.

983 Kuzucuoğlu, C Bertaux, J., Black, S., Denefle, M., Fontugne, M., Karabiyikoğlu, M., Kashima,
984 K., Limondin-Lozouet, N., Mouralis, D., Orth, P.J.G.J., 1999. Reconstruction of climatic
985 changes during the Late Pleistocene, based on sediment records from the Konya Basin
986 (Central Anatolia. Turkey), Geological Journal, 34, Special Issue: Advances in Turkish
987 Geology, Part I, 175–198.
988 Kuzucuoğlu, C., Christol, A., Mouralis, D., Doğu, A.F., Akköprü, E., Fort, M., Brunstein, D.,
989 Zorer, H., Fontugne, M., Karabiyikoğlu, M., 2010. Formation of the upper pleistocene
990 terraces of Lake Van (Turkey). Journal of Quaternary Science 25, 1124-1137.
991 Kwiecien, O., Arz, H.W., Lamy, F., Plessen, B., Bahr, A., Haug, G.H., 2009. North Atlantic
992 control on precipitation pattern in the eastern Mediterranean/Black Sea region during the
993 last glacial. Quaternary Research 71, 375-384.
994 Kwiecien, O., Stockhecke, M., Pickarski, N., Heumann, G., Litt, T., Sturm, M., Anselmetti, F.,
995 Kipfer, R., Haug, G.H., 2014. Dynamics of the last four glacial terminations recorded in
996 Lake Van, Turkey. Quaternary Science Reviews 104, 42-52.
997 Kylander, M.E., Ampel, L., Wohlfarth, B., Veres, D., 2011. High-resolution X-ray
998 fluorescence core scanning analysis of Les Echets (France) sedimentary sequence: new
999 insights from chemical proxies. Journal of Quaternary Science 26, 109-117.
1000 Le Pape, P., Battaglia-Brunet, F., Parmentier, M., Joulian, C., Gassaud, C., Fernandez-Rojo,
1001 L., Guigner, J.-M., Ikogou, M., Stetten, L., Olivi, L., 2017. Complete removal of arsenic
1002 and zinc from a heavily contaminated acid mine drainage via an indigenous SRB
1003 consortium. Journal of Hazardous Materials 321, 764-772.

1004 Major, C., Ryan, W., Lericolais, G., Hajdas, I., 2002. Constraints on Black Sea outflow to the
1005 Sea of Marmara during the last glacial–interglacial transition. Marine Geology 190, 19-
1006 34.
1007 Mayewski, P.A., Rohling, E.E. Stager, C., Karlén, W., Maasch, K.A., Meeker, L.D., Meyerson,
1008 E.A., Gasse, F., van Kreveld, S., Holmgren, K., Lee-Thorp, J., Rosqvist, G., Rack, F.,
1009 Staubwasser, M., Schneider, R.R., Steig, E.J., 2004. Holocene climate variability,
1010 Quaternary Research, 62, 243-255.
1011 Migowski, C., Stein, M., Prasad, S., Negendank, J.F., Agnon, A., 2006. Holocene climate
1012 variability and cultural evolution in the Near East from the Dead Sea sedimentary record.
1013 Quaternary Research 66, 421-431.
1014 Neugebauer, I., Schwab, M., Waldmann, N.D., Tjallingii, R., Frank, U., Hadzhiivanova, E.,
1015 Naumann, R., Taha, N., Agnon, A., Enzel, Y., 2016. Hydroclimatic variability in the
1016 Levant during the early last glacial (~ 117–75 ka) derived from micro-facies analyses of
1017 deep Dead Sea sediments. Climate of the Past 12, 75-90.
1018 NGRIP - North Greenland Ice Core Project Members, 2004. High-resolution record of
1019 Northern Hemisphere climate extending into the last interglacial period. Nature 431, 147-
1020 151.
1021 Ön, Z.B., Akçer-Ön, S., Özeren, M.S., Eriş, K.K., Greaves, A.M., Çağatay, M.N., 2018.
1022 Climate proxies for the last 17.3 ka from Lake Hazar (Eastern Anatolia), extracted by
1023 independent component analysis of μ-XRF data. Quaternary International 486, 17-28.
1024 Peinerud, E.K., 2000. Interpretation of Si concentrations in lake sediments: three case studies.
1025 Environmental Geology 40, 64-72.

1026 Peti, L., Augustinus, P.C., 2022. Micro-XRF-inferred depositional history of the Orakei maar
1027 lake sediment sequence, Auckland, New Zealand. Journal of Paleolimnology 67, 327-344.
1028 Roberts, A.P., 1995. Magnetic properties of sedimentary greigite (Fe3S4). Earth and Planetary
1029 Science Letters 134, 227-236.
1030 Roberts, N., Jones, M., Benkaddour, A., Eastwood, W., Filippi, M., Frogley, M., Lamb, H.,
1031 Leng, M., Reed, J., Stein, M., 2008. Stable isotope records of Late Quaternary climate and
1032 hydrology from Mediterranean lakes: the ISOMED synthesis. Quaternary Science
1033 Reviews 27, 2426-2441.
1034 Roberts, N., Reed, J., Leng, M., Kuzucuoğlu, C., Fontugne, M., Bertaux, J., Woldring, H.,
1035 Bottema, S., Black, S., Hunt, E., 2001. The tempo of Holocene climatic change in the
1036 eastern Mediterranean region: new high-resolution crater-lake sediment data from central
1037 Turkey. The Holocene 11, 721-736.
1038 Rodriguez-Freire, L., Moore, S.E., Sierra-Alvarez, R., Root, R.A., Chorover, J., Field, J.A.,
1039 2016. Arsenic remediation by formation of arsenic sulfide minerals in a continuous
1040 anaerobic bioreactor. Biotechnology and Bioengineering 113, 522-530.
1041 Shahrabi, M., 1981. Holocene lacustrine facies and climatic cycles in the hypersaline lake
1042 Urmieh Basin, Northwest Iran, Diplomarb. Abt. Naturwiss. ETH Zürich.
1043 Sharifi, A., Shah-Hosseini, M., Pourmand, A., Esfahaninejad, M., Haeri-Ardakani, O., 2018.
1044 The Vanishing of Urmia Lake: a geolimnological perspective on the hydrological
1045 imbalance of the world's second largest hypersaline lake. The Handbook of
1046 Environmental Chemistry, pp. 1-38.

1047 Sharifi, A., Pourmand, A., Canuel, E.A., Ferer-Tyler, E., Peterson, L.C., Aichner, B., Feakins,
1048 S.J., Daryaee, T., Djamali, M., Beni, A.N., Lahijani, H.A.K., Swart, P.K., 2015. Abrupt
1049 climate variability since the last deglaciation based on a high-resolution, multi-proxy peat
1050 record from NW Iran: The hand that rocked the Cradle of Civilization? Lake Neor.
1051 Quaternary Science Reviews 123, 215-230.
1052 Smedley, P.L., Kinniburgh, D.G., 2002. A review of the source, behaviour and distribution of
1053 arsenic in natural waters. Applied geochemistry 17, 517-568.
1054 Solaymani Azad, S., 2009. Evaluation de l'aléa sismique pour les villes de Téhéran, Tabriz et
1055 Zandjan dans le NW de l'Iran: approche morphotectonique et paléosismologique,
1056 Montpellier 2, Doctoral dissertation.
1057 Soulet, G., Ménot, G., Garreta, V., Rostek, F., Zaragosi, S., Lericolais, G., Bard, E., 2011.
1058 Black Sea "Lake" reservoir age evolution since the Last Glacial—Hydrologic and climatic
1059 implications. Earth and Planetary Science Letters 308, 245-258.
1060 Stappen, G.V., Fayazi, G., Sorgeloos, P., 2001. International study on Artemia LXIII. Field
1061 study of the Artemia urmiana (Günther, 1890) population in Lake Urmiah, Iran, Saline
1062 Lakes. Springer, pp. 133-143.
1063 Staubwasser, M., Weiss, H., 2006. Holocene climate and cultural evolution in late prehistoric–
1064 early historic West Asia. Quaternary Research 66, 372-387.
1065 Stein, M., Starinsky, A., Katz, A., Goldstein, S.L., Machlus, M., Schramm, A., 1997. Strontium
1066 isotopic, chemical, and sedimentological evidence for the evolution of Lake Lisan and the
1067 Dead Sea. Geochimica et Cosmochimica Acta 61, 3975-3992.

1068 Stein, M., Torfstein, A., Gavrieli, I., Yechieli, Y., 2010. Abrupt aridities and salt deposition in
1069 the post-glacial Dead Sea and their North Atlantic connection. Quaternary Science
1070 Reviews 29, 567-575.
1071 Stevens, L.R., Djamali, M., Andrieu-Ponel, V., de Beaulieu, J.L., 2012. Hydroclimatic
1072 variations over the last two glacial/interglacial cycles at Lake Urmia, Iran. Journal of
1073 Paleolimnology 47, 645-660.
1074 Stevens, L.R., Ito, E., Schwalb, A., Wright, H.E., 2006. Timing of Atmospheric Precipitation
1075 in the Zagros Mountains Inferred from a Multi-Proxy Record from Lake Mirabad, Iran.
1076 Quaternary Research 66, 494-500.
1077 Stevens, L.R., Wright, H.E., Ito, E., 2001. Proposed changes in seasonality of climate during
1078 the Lateglacial and Holocene at Lake Zeribar, Iran. The Holocene 11, 747-755.
1079 Talebi, T., Ramezani, E., Djamali, M., Lahijani, H.A.K., Naqinezhad, A., Alizadeh, K.,
1080 Andrieu-Ponel, V., 2016. The Late-Holocene climate change, vegetation dynamics, lake-
1081 level changes and anthropogenic impacts in the Lake Urmia region, NW Iran. Quaternary
1082 International 408, 40-51.
1083 Tourian, M., Elmi, O., Chen, Q., Devaraju, B., Roohi, S., Sneeuw, N., 2015. A spaceborne
1084 multisensor approach to monitor the desiccation of Lake Urmia in Iran. Remote Sensing
1085 of Environment 156, 349-360.
1086 J. Trichet, J., Défarge, C., Tribble, J., Tribble, G., Sansone, F., 2001. Christmas Island lagoonal
1087 lakes, models for the deposition of carbonate-evaporite-organic laminated sediments,
1088 Sedimentary Geology, 140, 177-189.

1089 Tudryn, A., Gibert-Brunet, E., Tucholka, P., Antipov, M.P., Leroy, S.A.G., 2022. Chronology
1090 of the Late Pleistocene Caspian Sea hydrologic changes: A review of dates and proposed
1091 climate-induced driving mechanisms, Quaternary Science Reviews 293, 107672.
1092 Tudryn, A., Motavalli-Anbaran, S.H., Tucholka, P., Gibert-Brunet, E., Lankarani, M.,
1093 Ahmady-Birgani, H., Kong, T., Noret, A., Miska, S., Massault, M., Dufaure, O., 2021.
1094 Late Quaternary environmental changes of Lake Urmia basin (NW Iran) inferred from
1095 sedimentological and magnetic records. Quaternary International 589, 83-94.
1096 Tudryn, A., Tucholka, P., Özgûr, N., Gibert, E., Elitok, O., Kamaci, Z., Massault, M., Poisson,
1097 A., Platevoet, B., 2013. A 2300-year record of environmental change from SW Anatolia,
1098 Lake Burdur, Turkey. Journal of paleolimnology 49, 647-662.
1099 Tudryn, A., Tucholka, P., Gibert, E., Gasse, F., Wei, K., 2010. A late Pleistocene and Holocene
1100 mineral magnetic record from sediments of Lake Aibi, Dzungarian Basin, NW China.
1101 Journal of Paleolimnology 44, 109-121.
1102 Turner, R., Roberts, N., Jones, M., 2008. Climatic pacing of Mediterranean fire histories from
1103 lake sedimentary microcharcoal. Global and Planetary Change 63, 317-324.
1104 Wang, H., Göttlicher, J., Byrne, J., Guo, H., Benning, L.G., Norra, S., 2021. Vertical redox
1105 zones of Fe–S–As coupled mineralogy in the sediments of Hetao Basin–Constraints for
1106 groundwater As contamination. Journal of Hazardous Materials 408, 124924.
1107 Wasylikowa, K., Witkowski, A., Walanus, A., Hutorowicz, A., Alexandrowicz, S.W., Langer,
1108 J.J., 2006. Palaeolimnology of Lake Zeribar, Iran, and its climatic implications.
1109 Quaternary Research 66, 477-493.

1110 Wei, G., Liu, Y., Li, X., Shao, L., Liang, X., 2003. Climatic impact on Al, K, Sc and Ti in
1111 marine sediments: evidence from ODP site 1144, South China Sea, Geochemical Journal,
1112 37, 593-602.
1113 Weltje, G. J. and Tjallingii, R., 2008. Calibration of XRF core scanners for quantitative
1114 geochemical logging of sediment cores: Theory and application, Earth and Planetary
1115 Science Letters, 274, 423-438.
1116 Weltje, G. J., Bloemsma, M.R., Tjallingii, R., Heslop, D., Röhl, U., Croudace, I.W., 2015.
1117 Prediction of Geochemical Composition from XRF Core Scanner Data: A New
1118 Multivariate Approach Including Automatic Selection of Calibration Samples and
1119 Quantification of Uncertainties, In book: Micro-XRF studies of sediment cores, Chapter
1120 21: 507-534, Springer Editors: I.W. Croudace and R.G. Rothwell.
1121 Wurtsbaugh, W.A., Gliwicz, Z.M., 2001. Limnological control of brine shrimp population
1122 dynamics and cyst production in the Great Salt Lake, Utah, Saline Lakes. Springer, pp.
1123 119-132.
1124 Xie, X., Zheng, H.B., Qiao, P.J., 2014. Millennial climate changes since MIS 3 revealed by
1125 element records in deep-sea sediments from northern South China Sea. Chinese Science
1126 Bulletin 59, 776-784.
1127 Xu, H., Liu, B., Wu, F., 2010. Spatial and temporal variations of Rb/Sr ratios of the bulk surface
1128 sediments in Lake Qinghai. Geochemical Transactions 11, 1-8.
1129

1130 Figure captions

1131

1132 Fig. 1. Lake Urmia: (a) location of the lake (b) the lake's catchment area: the blue lines
1133 delimiting Lake Urmia catchment area (Aubert et al., 2017); (c) simplified geological map of
1134 the Lake Urmia catchment area (according to Sharifi et al., 2018, as modified by Tudryn et al,
1135 2021); (d) location of the coring site: the black circles indicate the Golman 5, Golman 6 and
1136 Golman 7 coring sites; support from Google Earth.

1137

1138 Fig. 2. Down-core variation of simplified lithofacies and lithological units from the Lake Urmia
1139 composite sediment-core (Golman 6 and Golman 7 cores – see location shown in Fig. 1), details
1140 of the ^{14}C AMS dating methodology including: depth of sample analysis, dated material,
1141 measured age, calibrated age, mean sedimentary rate and the age-depth model for the
1142 composite core obtained using ^{14}C ages. For further details, see Kong et al. (2022).
1143 Abbreviations: OM – organic matter, White FP – white shrimp fecal pellet, (G7) - Golman 7
1144 core, (G6) - Golman 6 core. Before calibration, measured ^{14}C ages were corrected: * from the
1145 detrital carbonate fraction, ▵ from the 2-kyr hard water effect.

1146 .

1147 Fig. 3. Elemental XRF-CS data in Lake Urmia sediments: (a) correlation index between
1148 elements: Mg, Al, Si, P, S, Cl, K, Ca, Ti, Mn, Fe, As, Ni, Cu, Zn, Br, Rb, Sr and Zr, (b) principal
1149 component analysis (PCA) plot, (c) Si *versus* Al, (d) Sr *versus* Ca, and (e) S *versus* Ca.

1150

Fig. 4. Elemental XRF-CS and mineralogical data from the Lake Urmia composite core by ^{14}C age: (a) ln of Si *versus* Ca, (b) ln of Rb *versus* Sr, (c) quartz percentages in bulk samples, (d) mean sediment grain size, (e) ln of K *versus* Ti, (f) illite percentages in bulk samples and (g) grain-size fraction from 0 to 10 μm. Mineralogical and grain size data (c, d, f and g) and chronology according to Kong et al. (2022). Lithological units as in Fig. 2.

Fig. 5. Elemental XRF-CS and mineralogical data from the Lake Urmia composite core by ^{14}C age: (a) ln of Ca *versus* Ti, (b) Ca intensity, (c) carbonate and aragonite content in bulk samples, (d) ln of Sr v*ersus* Ca, (e) ln of Cl *versus* Sr, (f) ln of Cl *versus* S, (g) halite percentages in bulk samples. Carbonate contents (c) and chronology according to Kong et al. (2022). Lithological units as in Fig. 2.

Fig. 6. Elemental XRF-CS and mineralogical data from the Lake Urmia composite core by ^{14}C age: (a) gypsum content in bulk samples, (b) ln of S *versus* Ca, (c) magnetic susceptibility and mineralogy, (d) Arsenic intensity. Magnetic susceptibility and mineralogy (c) according to Tudryn et al. (2021), chronology according to Kong et al. (2022). Blue arrow corresponds to gypsum peak, red arrow shows correlation between peaks of sulfur, arsenic and magnetic susceptibility. Lithological units as in Fig. 2.

Fig. 7. X-ray diffraction pattern obtained for the magnetic extract from the Golman 5 core at 2.50 m in depth with mean identified minerals: arsenopyrite (As), which is highlighted by

1172 vertical green lines, greigite (Gr), albite (Al), calcite (Ca), chlorite (Ch), muscovite (Mu), pyrite
1173 (Py), quartz (Qu). According to Tudryn et al. (2021).
1174
1175 Fig. 8. Elemental XRF-CS profile by ^{14}C age: (a) Lake Urmia: ln of Ca *versus* Ti, focus on
1176 interval 30.0-20.0 and 5.0-2.0 cal kBP, (b) Lake Urmia: ln of Ca *versus* Ti, the full sequence,
1177 (c) Ca in Lake Hazar sediments (Ön et al., 2018), (d) ratio of Ca *versus* Fe in North Basin
1178 sediments from Lake Van (Çağatay et al., 2014), (e) ratio of Ca *versus* K in Ahlat Ridge
1179 sediments from Lake Van (Kwiecien et al., 2014; Pickarski et al., 2015), (f) Ca in Black Sea
1180 sediments (Constantinescu et al., 2015; Soulet et al., 2011), and (g) NGRIP curve (NGRIP,
1181 2004). Abbreviations: YD - Younger Dryas cooling, B-A – Bølling-Allerød warming, LGM –
1182 Last Glacial Maximum, D-O3 and D-O4 - Dansgaard–Oeschger events 4 and 3.

Graphical Abstract

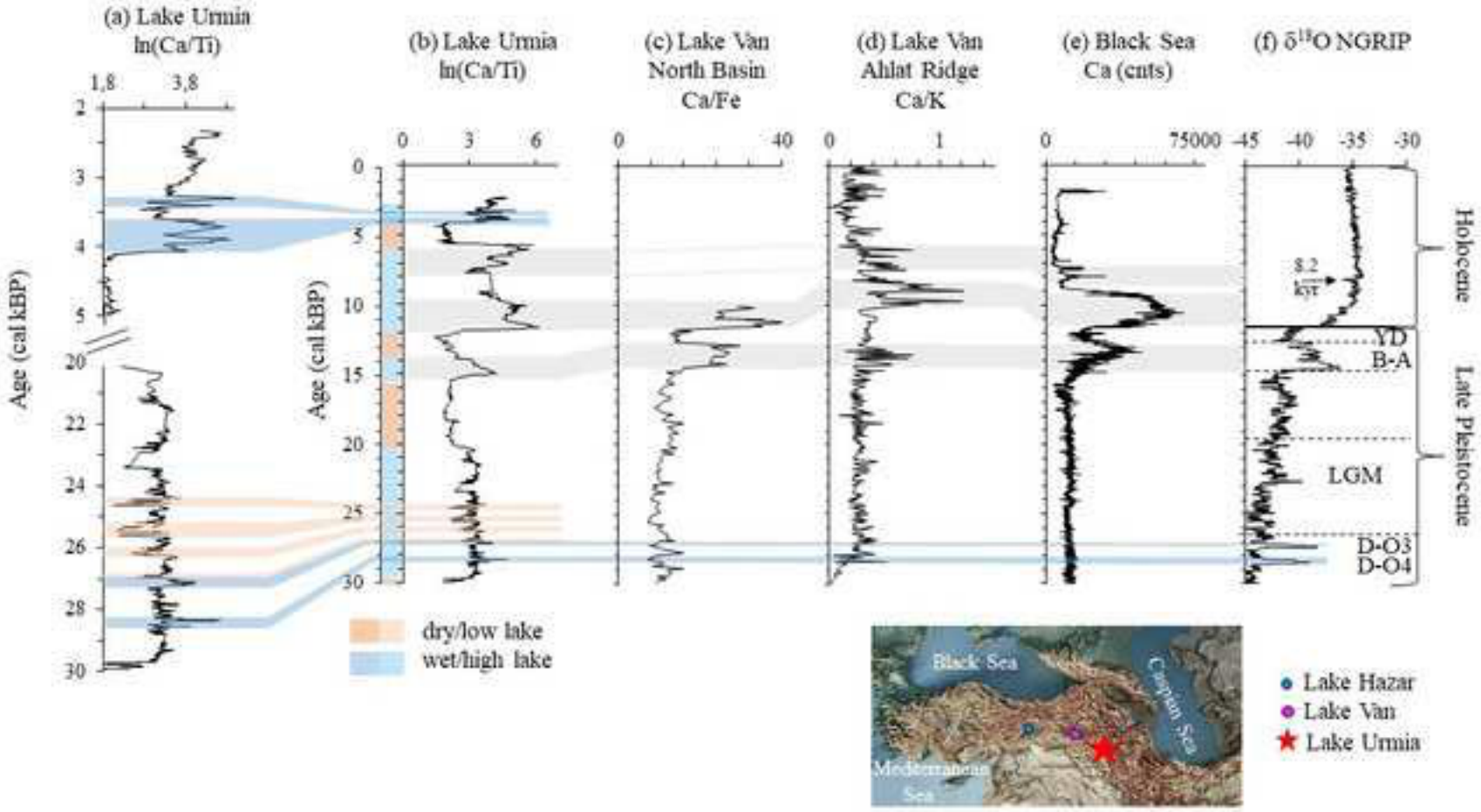

1 Last 30 kyr lake evolution; wet LGM and Early Holocene, dry Mid to Late Holocene.
2 Erosion/chemical weathering in the catchment and carbonate crystallization in the lake.
3 Arsenic of natural origin and iron sulfides show anoxic depositional conditions.
4 Unique record on W Asia paleoclimate and data for global paleoclimate reconstructions.
5 Short-term climate variations correlated to Dansgaard-Oeshger events 4 and 3.
6 Last 30 kyrs of long and short term climate change related to North Atlantic system.

Figure 1

Click here to access/download;Figure;Fig 1 -KONG et al_XRF march 2023.jpg

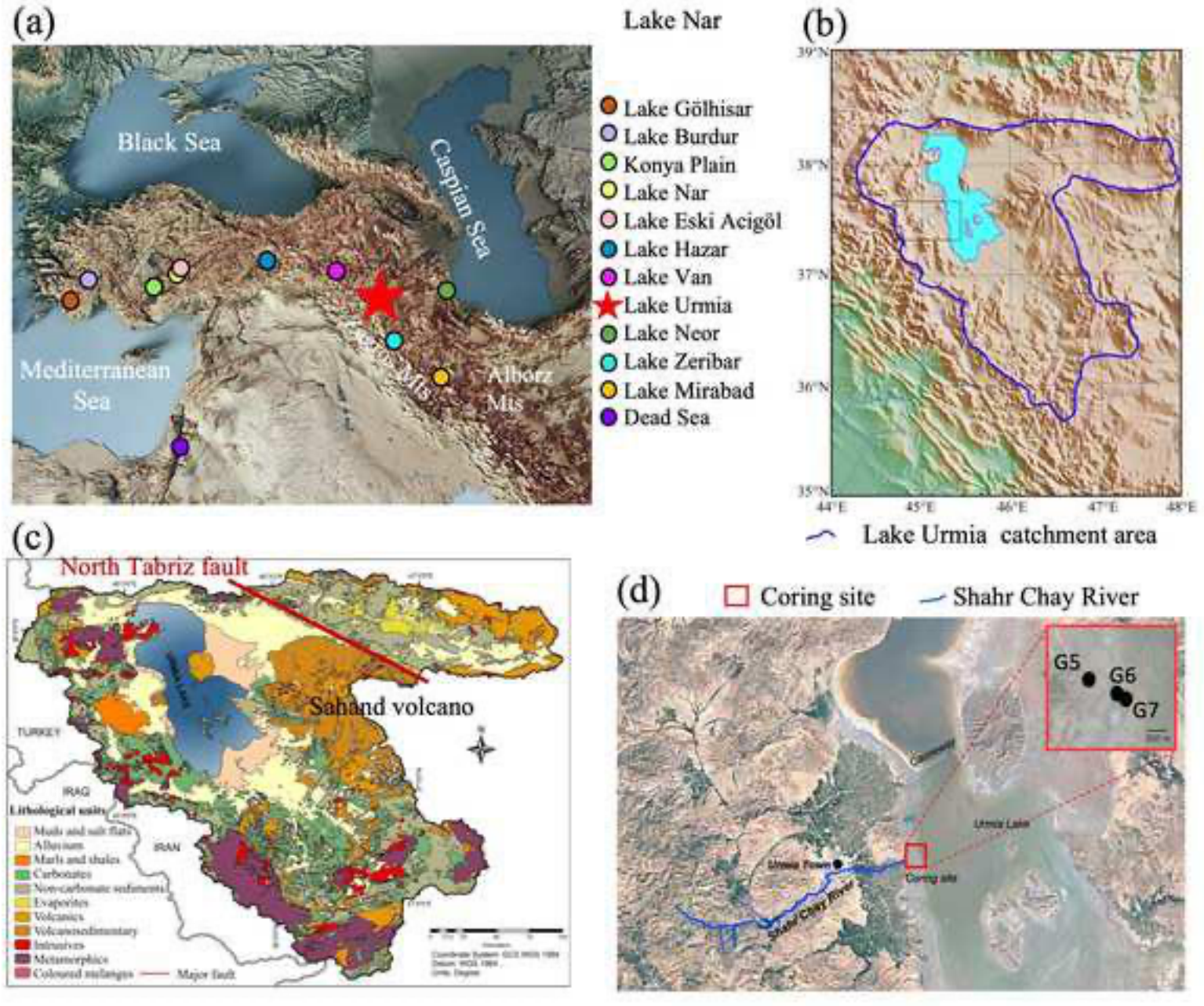

Figure 2

Click here to access/download;Figure;Figure 2.jpg

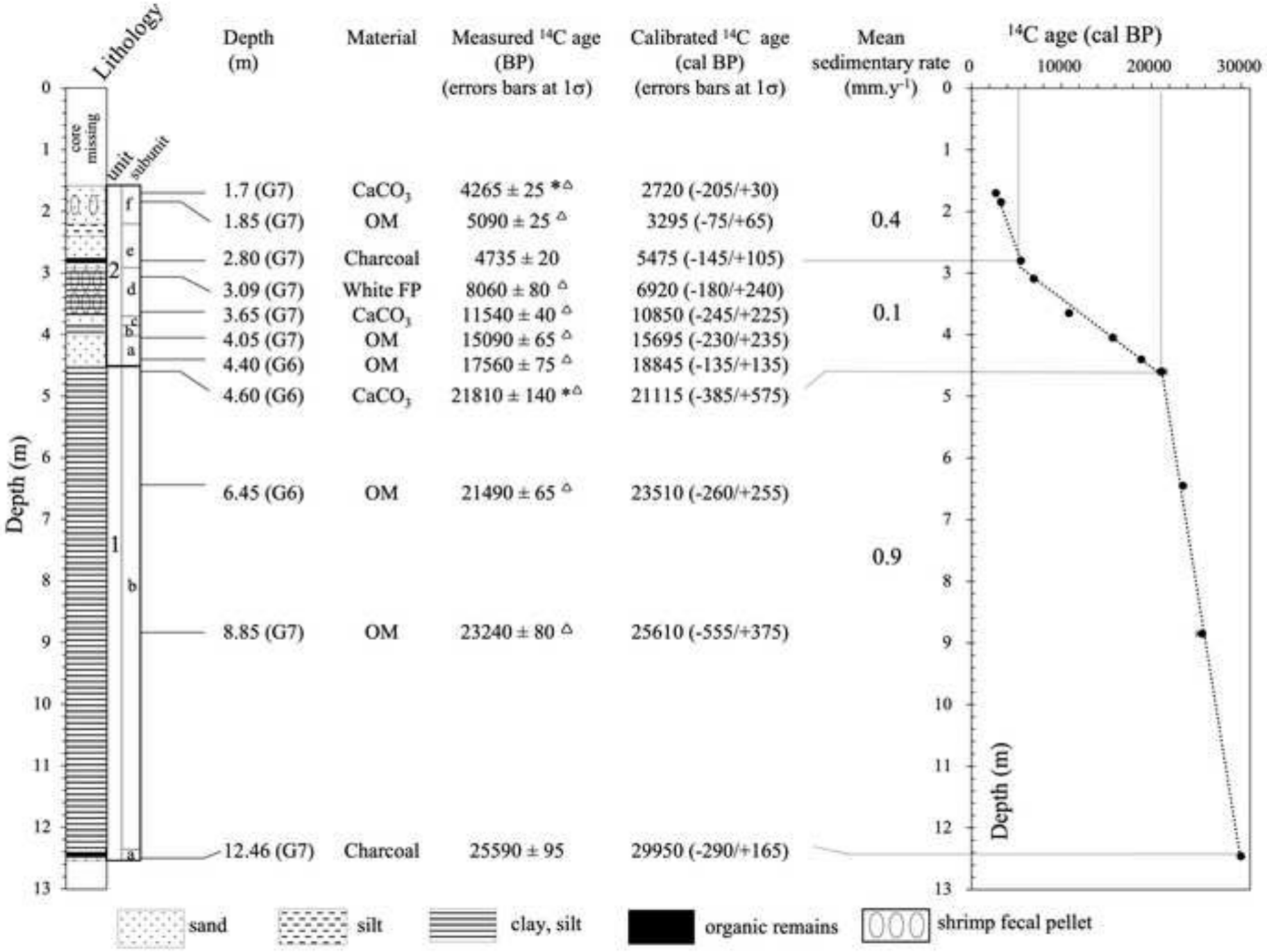

Figure 3

Click here to access/download;Figure;Fig 3-KONG et al_XRF-march 2023.jpg

(a)

	Mg	Al	Si	P	S	Cl	K	Ca	Ti	Mn	Fe	As	Ni	Cu	Zn	Br	Rb	Sr	Zr
Mg	1																		
Al	0.895	1																	
Si	0.860	0.985	1																
P	0.650	0.691	0.673	1															
S	-0.343	-0.419	-0.462	-0.162	1														
Cl	-0.052	-0.256	-0.281	-0.062	0.166	1													
K	0.850	0.965	0.963	0.654	-0.471	-0.154	1												
Ca	0.332	0.184	0.119	0.494	0.242	0.171	0.068	1											
Ti	0.613	0.795	0.824	0.460	-0.475	-0.105	0.883	-0.238	1										
Mn	0.756	0.785	0.776	0.646	-0.401	0.018	0.825	0.216	0.744	1									
Fe	0.789	0.890	0.893	0.626	-0.464	-0.076	0.954	0.014	0.907	0.875	1								
As	-0.170	-0.207	-0.233	-0.009	0.296	0.219	-0.217	0.173	-0.250	-0.192	-0.202	1							
Ni	0.740	0.740	0.724	0.713	-0.270	0.045	0.741	0.457	0.539	0.750	0.722	-0.018	1						
Cu	0.543	0.650	0.651	0.578	-0.323	-0.045	0.691	0.175	0.604	0.622	0.671	-0.073	0.674	1					
Zn	0.700	0.816	0.822	0.559	-0.448	-0.074	0.883	-0.038	0.857	0.781	0.899	-0.133	0.700	0.692	1				
Br	0.469	0.355	0.310	0.440	0.011	0.579	0.374	0.414	0.264	0.506	0.403	0.135	0.576	0.363	0.376	1			
Rb	0.316	0.504	0.547	0.071	-0.433	-0.130	0.620	-0.612	0.772	0.356	0.614	-0.261	0.173	0.329	0.623	-0.003	1		
Sr	-0.022	-0.189	-0.258	0.182	0.369	0.246	-0.299	0.865	-0.525	-0.130	-0.341	0.272	0.113	-0.118	-0.369	0.242	-0.756	1	
Zr	0.000	0.125	0.166	-0.106	-0.220	-0.041	0.207	-0.520	0.497	0.096	0.257	-0.169	-0.099	0.047	0.247	-0.089	0.570	-0.514	1

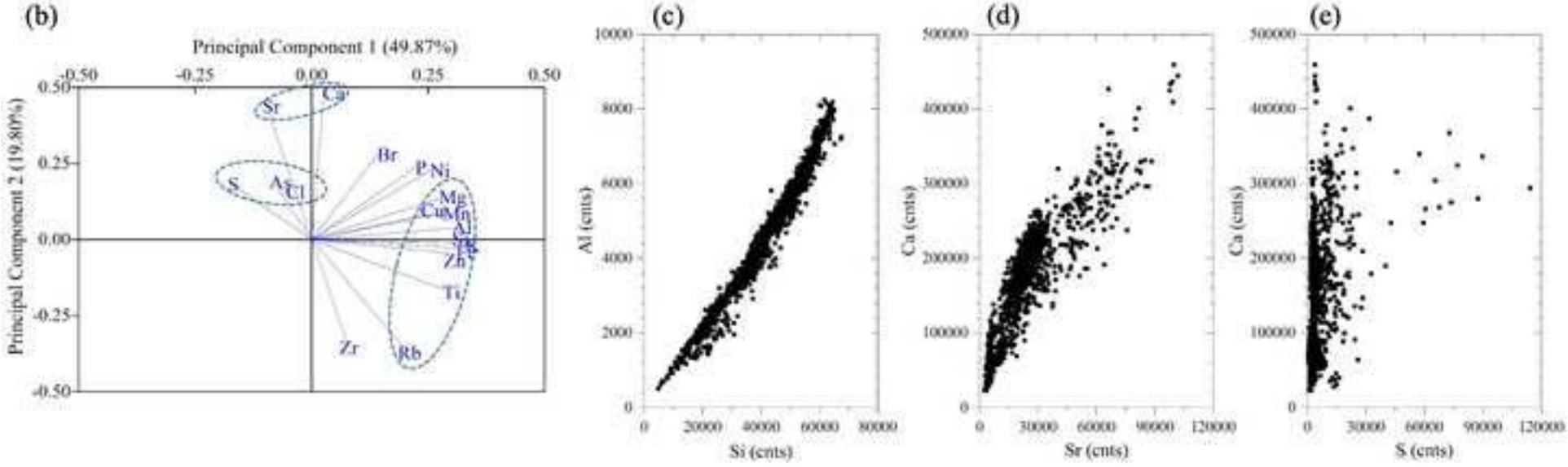

Figure 4

Click here to access/download;Figure;Figure 4.jpg

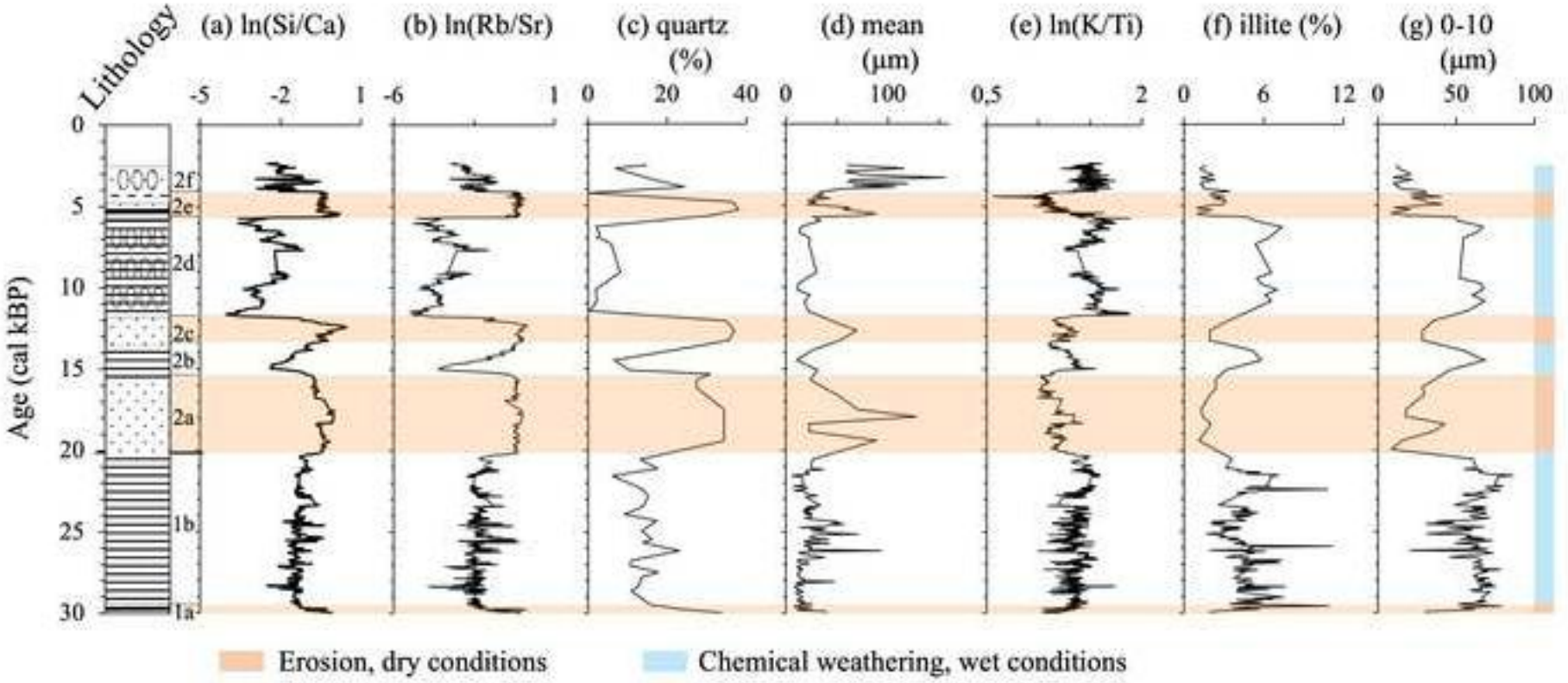

Figure 5

Click here to access/download;Figure;Figure 5.jpg

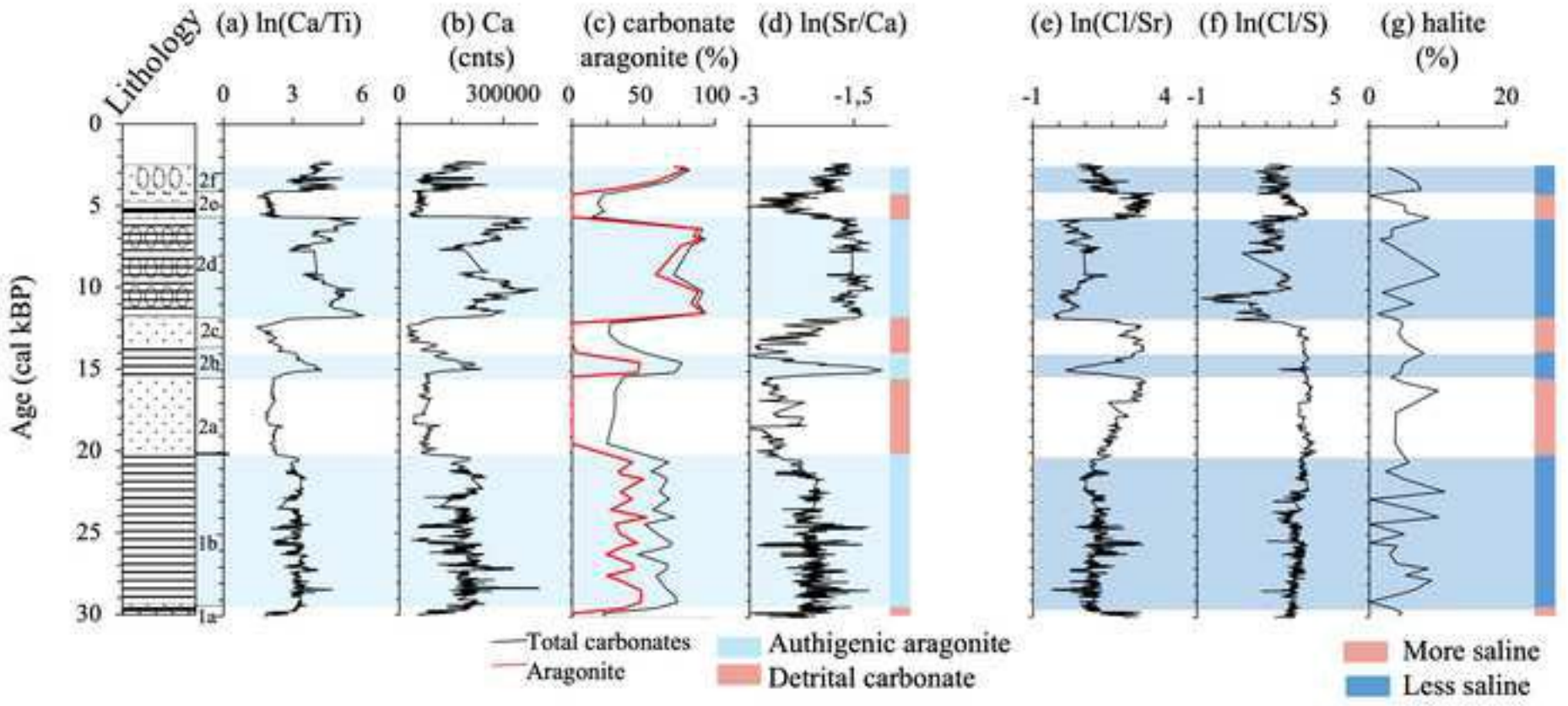

Figure 6

Click here to access/download;Figure;Figure 6.jpg

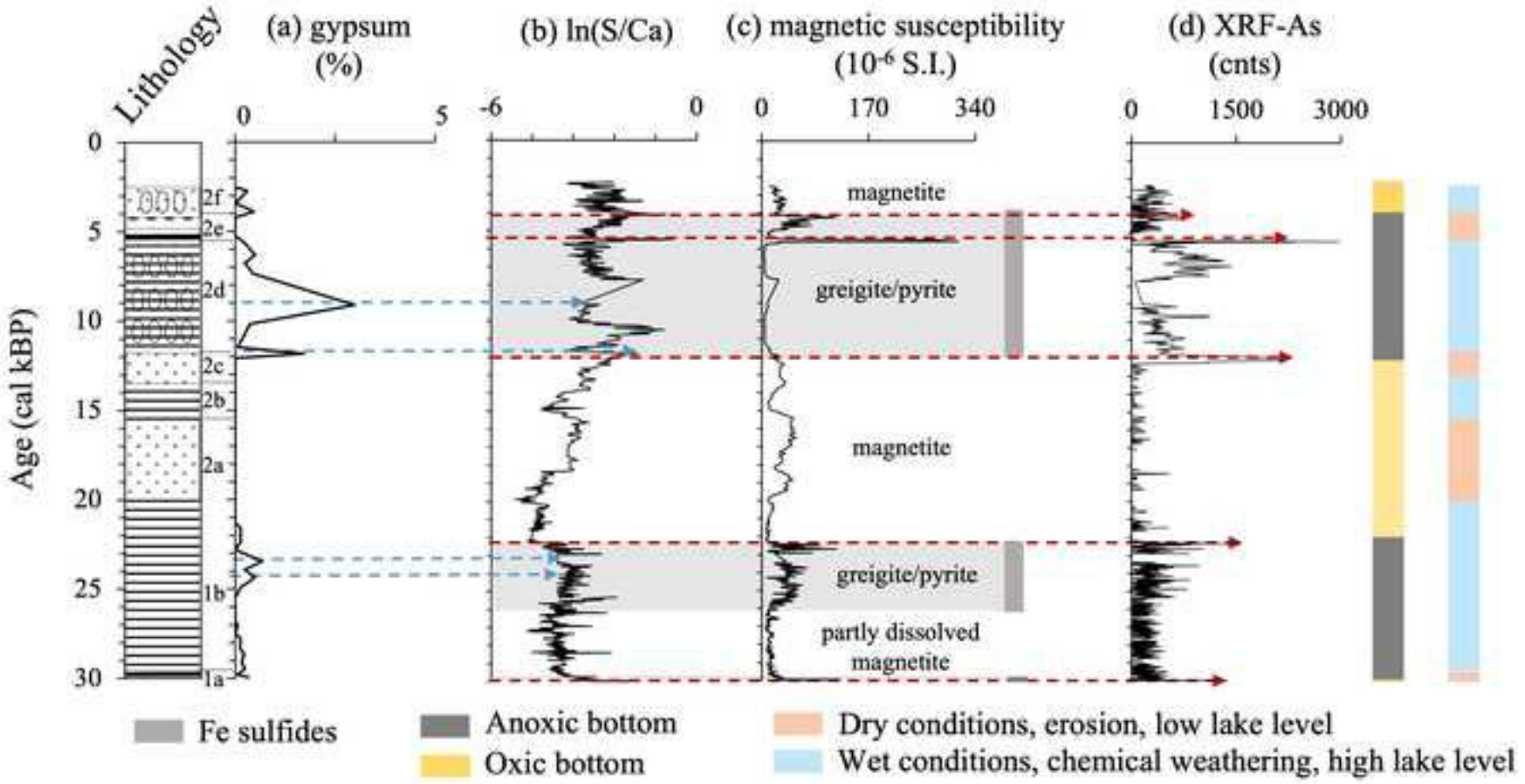

Figure 7

Click here to access/download;Figure;Fig 7-KONG et al_XRF-marcg 2023.jpg

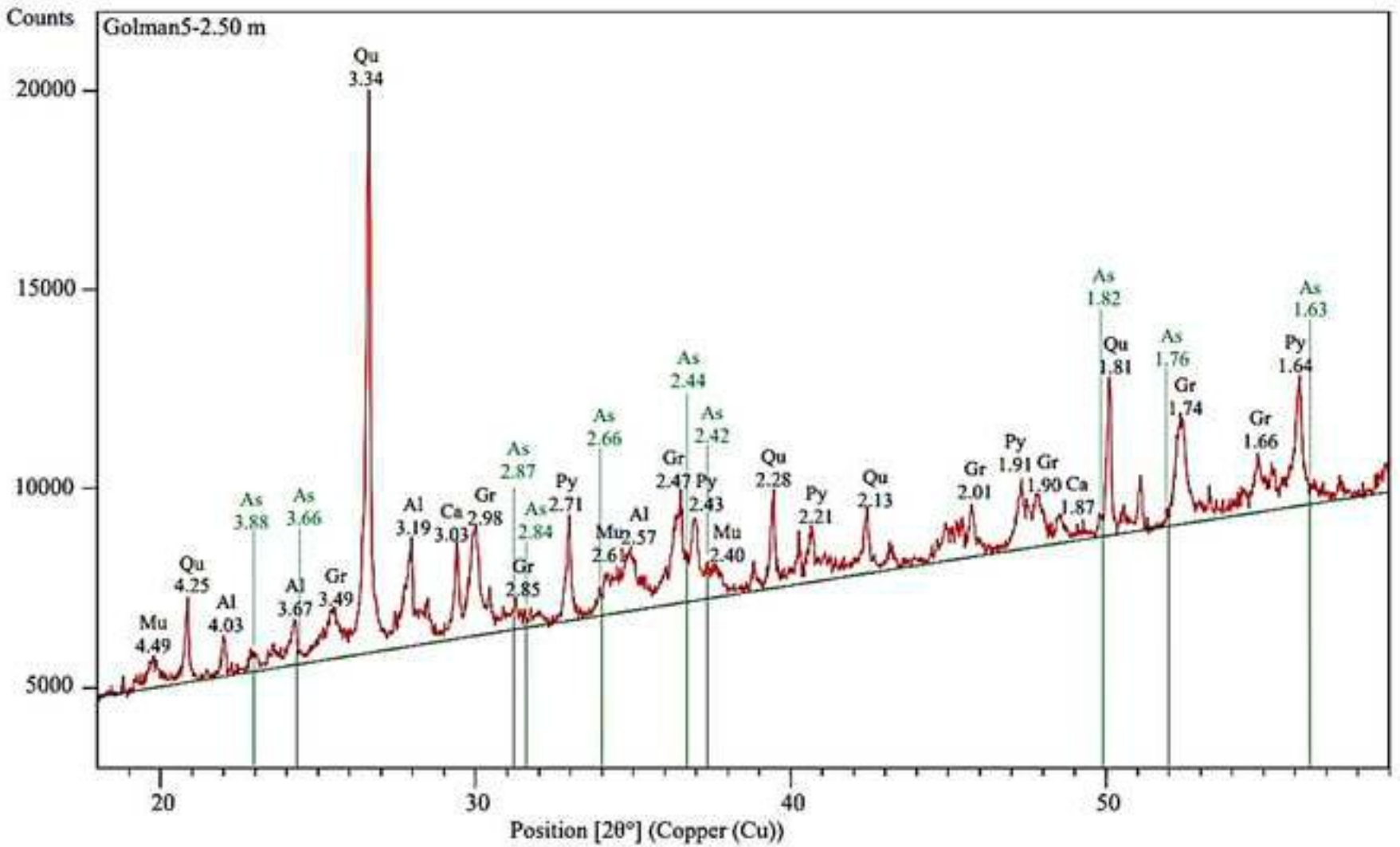

Figure 8

Click here to access/download;Figure;Figure 8.jpg